Statistics of bubble plumes generated by breaking surface waves

Morteza Derakhti[1], Jim Thomson[1], Christopher Bassett[1], Mika Malila[2], and James T. Kirby[3]

[1]Applied Physics Laboratory, University of Washington, Seattle, WA, USA
[2]Institute of Marine Sciences, University of North Carolina at Chapel Hill, Morehead City, NC, USA
[3]Center for Applied Coastal Research, Department of Civil and Environmental Engineering, University of Delaware, Newark, DE, USA

Key Points:

- Bubble plumes generated during ocean surface wave breaking are observed with echosounders on drifting buoys.
- Bubble plume depths are well correlated with whitecap coverage, wind speed, and spectral wave steepness.
- Bubble plumes persist for many wave periods and exceed the persistence of visible surface foam.

Corresponding author: Morteza Derakhti, `derakhti@uw.edu`

Abstract

We examine the dependence of the penetration depth and fractional surface area (e.g., whitecap coverage) of bubble plumes generated by breaking surface waves on various wind and wave parameters over a wide range of sea state conditions in the North Pacific Ocean, including storms with sustained winds up to 22 ms^{-1} and significant wave heights up to 10 m. Observations include arrays of freely drifting SWIFT buoys together with shipboard wind and optical video systems, which enabled concurrent high-resolution measurements of wind, waves, bubble plumes, and turbulence. We estimate bubble plume penetration depth from echograms that extend to more than 30 m depth in a surface-following reference frame collected by downward-looking echosounders integrated onboard the buoys. Our observations indicate that the mean and maximum bubble plume penetration depths exceed 10 m and 30 m beneath the surface at high winds, respectively, with a plume residence time of many wave periods. Bubble plume depths are well correlated with wind speeds, spectral wave steepness, and whitecap coverage. Plume depths scaled by total significant wave height are strongly linearly correlated with the inverse of wave age. Plume depths scaled by either wind sea or total significant wave height vary non-monotonically with increasing wind speeds. Dependencies of the combined observations on various non-dimensional predictors used for whitecap coverage estimation are also explored. This study provides first field evidence of a direct relation between bubble plume penetration depth and whitecap coverage, suggesting that the volume of bubble plumes could be estimated by remote sensing.

Plain Language Summary

Quantifying the statistics of bubble plumes generated during ocean surface wave breaking is essential to understand the exchange between the ocean and the atmosphere. Bubble plumes also cause important variations in underwater acoustics and optics. Recent studies also suggest that the statistics of bubble plumes are skillful predictors for total energy loss during wave breaking, which is an essential quantity for accurate wave forecasting. Here we examine the dependence of bubble plume statistics on various wind and wave parameters over a wide range of sea state conditions, including storms. Echosounders integrated onboard drifting buoys are used to detect bubbles and estimate their penetration depth below the ocean surface. Visible surface area of these bubble plumes is also observed using shipboard optical video systems. We successfully provide multiple empirical relationships that predict the observed variability of the penetration depth and surface area of bubble plumes as a function of simple wind and wave statistics (available from existing forecast models or typical ocean buoys). Our results indicate that the penetration depth of bubble plumes is correlated with their visible surface area, suggesting that the volume of bubble plumes could be estimated by observing the ocean surface from above.

1 Introduction

Air-entraining breaking surface waves play a significant role in air-sea exchanges of mass, heat, energy, and momentum [*Melville*, 1996; *Sullivan and McWilliams*, 2010; *Deike*, 2022], and are also crucial in various technical applications, such as the design of marine structures and underwater communications. Breaking waves inject a relatively large volume of air into the water column as bubbles which then form intermittent bubble clouds at a wide range of spatial scales, hereafter referred to as bubble plumes. The entrained bubbles change optical properties of the water column [*Terrill et al.*, 2001; *Al-Lashi et al.*, 2016] and generate acoustic noise [*Felizardo and Melville*, 1995; *Manasseh et al.*, 2006], especially during the active breaking period.

Quantifying the statistics of these bubble plumes (*e.g.,* void fractions, size distributions, penetration depth, surface area, and volume of bubble plumes averaged over many waves) is essential to obtain robust parameterizations of fluxes at the ocean-atmosphere interface and variations in underwater acoustics and optics. Recent studies, including the present observations, also show that the statistics of bubble plume that represent the overall size of bubble plumes are strongly correlated with total wave breaking dissipation [*Schwendeman and Thomson*, 2015a; *Callaghan et al.*, 2016; *Callaghan*, 2018; *Derakhti et al.*, 2020a]. This suggests that such bubble plume statistics are skillful predictors for the corresponding energy and momentum exchange between the ocean and atmosphere, especially in high sea states.

The statistics that represent the overall size of bubble plumes for a given sea state may be defined, in a wave-averaged sense, as the long-time (several minutes) average of the surface area and the penetration depth of individual bubble clouds. The former may be directly approximated from whitecap coverage W, which represents the average visible surface area of bubble plumes and surface foam patches per unit sea surface area. W is a reasonably easily measurable quantity using optical video systems. Estimation of bubble plume depth is, however, challenging and rare, especially during active wave breaking period. This study provides concurrent observations of W and bubble plume penetration depth in various sea states.

Many previous studies have examined the dependence of W on wind speeds and sea states [*Monahan and Muircheartaigh*, 1980; *Callaghan et al.*, 2008; *Kleiss and Melville*, 2010; *Schwendeman and Thomson*, 2015a; *Brumer et al.*, 2017; *Malila et al.*, 2022]. Despite large scatter in the data, particularly for wind speeds less than 10 ms^{-1}, these recent field studies have established fairly consistent empirical formulations that provide estimates of W based on given wind and/or sea state parameters.

Fewer previous studies reported mean values of the penetration depth of bubble plumes, $\overline{D}_{bp}$, for a range of wind speeds using upward-looking sonars moored to the sea bed or a platform [*Thorpe*, 1982, 1986; *Dahl and Jessup*, 1995; *Vagle et al.*, 2010; *Wang et al.*, 2016; *Strand et al.*, 2020]. These observations show that $\overline{D}_{bp}$ increases with increasing wind speed and varies from $[1-5]$ m at low winds to $[7-25]$ m during storms. However, the dependence of the statistics of D_{bp} on wind and sea state parameters is not well understood.

The main objective of this study is to understand and quantify the statistics that characterize the size of the bubble plumes (averaged over many waves, O(minutes)) generated by breaking surface waves in the open ocean. Our observations include arrays of freely drifting, surface-following SWIFT buoys together with shipboard wind and optical video systems, which enabled concurrent high-resolution measurements of wind, waves, whitecap coverage, bubble plumes, and turbulence over a wide range of sea state conditions in the North Pacific Ocean, including storms with sustained winds up to 22 ms^{-1} and significant wave heights up to 10 m. We estimate bubble plume penetration depth by using echograms that extend to more than 30 m depth in a surface-following reference frame using downward-looking echosounders integrated onboard the buoys.

We focus on examining the dependence of the statistics of the penetration depth of bubble plumes D_{bp} on various wind and wave parameters and the relation between D_{bp} statistics and W. Further, we comment on the role of wind history on W values. In a planned companion paper, we also investigate dynamic relationships between these bubble plume statistics and total wave breaking dissipation using our synchronized observations of bubble plumes and dissipation rates.

The rest of this paper is organized as follows: §2 describes the observed environmental conditions and our analysis for estimating bubble plume penetration depths. §3 describes the dependency of the bubble plume statistics on various wind and sea state parameters. Discussion and a summary of the main findings are provided in §4 and §5, respectively.

2 Methods

2.1 Data

The present data set includes observations of wind, waves, air and sea temperature, near-surface turbulence, time-depth images of acoustic backscatter (referred to as echograms), above- and sub-surface optical imagery by freely drifting surface following SWIFT buoys [*Thomson*, 2012; *Thomson et al.*, 2019], as well as concurrent shipboard measurements of wind, temperature, and whitecap coverage. The data were collected during an 18-day research cruise in the North Pacific Ocean (Figure A.1a) in December 2019. The primary objective of the cruise was to carry out concurrent observations of breaking surface gravity waves and the associated bubble plume statistics. The secondary objective was the replacement of a long-term moored wave buoy at Ocean Station PAPA (50° N, 145° W), which reports as CDIP 166 and NDBC 46246. Hereafter we refer to the present data set and cruise with the abbreviation PAPA.

The PAPA cruise, aboard the R/V *Sikuliaq*, departed Dutch Harbor, AK, on 5 December 2019 and ended in Seattle, WA, on 23 December 2019. Arrays of SWIFT buoys were deployed from the ship early in the morning and usually recovered later the same day. Most of the shipboard and autonomous measurements were carried out during local daylight hours, while the eastward transits were continued overnight. Figure A.1a shows the PAPA cruise track and average location of SWIFT buoys during each deployment along the transit. Figures A.1b, A.1c, and A.1d show that the PAPA data set includes a wide range of sea state conditions; U_{10N} (0.8–22 ms^{-1}), H_s (2.2 − 10.0 m), $T_m = f_m^{-1}$ (6.6 − 11.6 s), T_p (6.5 − 14.6 s), $T_{air} - T_{sea}$ (−4.4 to 1.2° C), c_m/U_{10N} (0.6–17.5), dU_{10N}/dt (−10.2 to 6.9 ms^{-1}/hr); including a storm in the vicinity of Station PAPA with sustained wind speeds up to 22 ms^{-1} and significant wave heights up to 10m. We note that a significant portion of the data was collected in the presence of persistent rain (though rain rates were not measured).

Raw SWIFT data were collected at sampling rates of 0.5–5 Hz in bursts lasting 512 seconds at intervals of 12 minutes. Processed SWIFT data, such as wave spectra and bubble plume statistics, are produced for each burst for each buoy, and then concurrent bursts are averaged among the buoys (typically 4 of them). During the cruise, more than 2000 bursts of data were collected by arrays of two to six SWIFT buoys, and 543 processed data points are obtained at intervals of 12 minutes spread over 14 daylight deployments. Statistics from the shipboard measurements, such as wind speeds and whitecap coverage, represent 10-minute average values and are obtained at the same time that the processed SWIFT data points are produced.

Two versions of SWIFT buoys have been concurrently used here, the version 3 buoys have uplooking Nortek Aquadopp Doppler sonars [*Thomson*, 2012], and the version 4 buoys have downlooking Nortek Signature1000 Doppler sonars which enable synchronous measurements of acoustic backscatter (i.e., echograms), broadband Doppler velocity profiles, and high-resolution (HR) turbulence profiles through the near-surface layer [*Thomson et al.*, 2019]. This new SWIFT capability allows us to quantify penetration depths of bubble plumes in a surface-following reference frame, with raw data that captures the time evolution within individual waves (i.e., phase-resolved).

The methodologies that we use to process echogram data and obtain bubble plume statistics are described in detail in this section. The instrumentation and methods that are used to obtain the rest of the relevant environmental variables and statistics, such as wind speeds, wave spectra, and whitecap coverage, are described in several previous observational studies [*Thomson*, 2012; *Schwendeman and Thomson*, 2015a; *Thomson et al.*, 2016, 2018], and will be briefly summarized here for convenience.

2.2 Wind Statistics

We calculate the neutral 10-m wind speed U_{10N} (Figure A.1b) following *Hsu* [2003] from wind speed measurements at 10 Hz, corrected for ship motion and airflow distortion, by three shipboard sonic anemometers (Metek Omni-3) at approximately 16.5 m height above the sea surface. The mean U_{10N} values are obtained over 10-minute bursts of raw data. We note that the atmospheric stability ($T_{air} - T_{sea}$) effect is often neglected in the estimation of the 10-m wind speed, or U_{10N} is simply approximated using the mean wind profile power law given by $U_{10}^{PL} = U_z(10/z)^{1/7}$. Figure A.1b shows the observed range of the shipboard measurements of $U_{10}^{PL} = U_{16.5}(10/16.5)^{1/7}$ (solid line) and the estimated U_{10N} values (circles) for the times that the processed SWIFT data are produced.

During the PAPA cruise, the atmospheric stability was negative most of the time ($T_{air}-T_{sea}$ ranged between -4.4 °C and 1.2 °C as shown in Figure A.1d) indicating unstable atmospheric boundary layer conditions. Figure A.2a shows that U_{10N} values are greater than U_{10}^{PL} in unstable atmospheric conditions by between 2% and 30%, where the differences decrease with increasing wind speed or $T_{air}-T_{sea}$ values. Figure A.2a also shows that the differences between U_{10N} and U_{10}^{PL} values are within 2% for stable atmospheric conditions (i.e., $T_{air} - T_{sea} > 0$).

The friction velocity u_* of the airflow is readily estimated from a modified logarithmic mean wind profile [*Hsu*, 2003], which accounts for atmospheric stability effects. The air-side friction velocity is also independently estimated using the inertial dissipation method and assuming neutral atmospheric stability as described in *Thomson et al.* [2018]; *Yelland et al.* [1994]. However, robust estimates of u_* are only achieved for a fraction of the time due to the strict requirements that the ship's heading is within 60 degrees of the wind and that the turbulent wind spectra match an expected frequency$^{-5/3}$ shape. Figure A.2b shows the two estimates of u_* against U_{10N} during the PAPA cruise. The mean u_* values are obtained over 10-minute bursts. The corresponding data from *Schwendeman and Thomson* [2015a], in which u_* values were estimated using the inertial dissipation method, are also compiled in Figure A.2b. Here we use the u_* values obtained from a modified logarithmic mean wind profile [*Hsu*, 2003] for all relevant analyses.

2.3 Wave Statistics

Wave spectral information, including the wave power spectral density $E(f)$ (m^{2}s) and frequency-dependent directional spread $\Delta\theta(f)$, are obtained by combining GPS and IMU measurements (collected by the SWIFT buoys) over the frequency range (0.01−0.49) Hz with a 0.012 Hz resolution as described in *Schwendeman and Thomson* [2015a]; *Thomson et al.* [2018]. As detailed below, several bulk and spectral wave parameters are then calculated using $E(f)$ and $\Delta\theta(f)$.

Figure A.2c shows examples of the observed $E(f)$, colored by U_{10N}, for $U_{10N} > 10$ ms^{-1}. The two vertical dotted lines in Figure A.2c show the equilibrium range $\sqrt{2} f_m$ to $\sqrt{5} f_m$, defined by *Schwendeman and Thomson* [2015a], over which the spectra approximately decay as f^{-4} consistent with the observations of *Schwendeman and Thomson* [2015a]. Here, f_m is the spectrally-weighted mean frequency given by

$$f_m = \frac{\int f E(f) df}{\int E(f) df}. \tag{1}$$

Figure A.2d shows the observed range of two commonly used alternatives for a characteristic wave period T, the peak wave period $T_p = f_p^{-1}$ and the mean wave period $T_m = f_m^{-1}$ (Eq. 1), as a function of U_{10N}. Figure A.2d also shows the wind sea mean wave period $T_m^{ws} = (f_m^{ws})^{-1}$, where f_m^{ws} calculated as given by Eq. 1 but over the wind sea portion of the observed wave spectra $E^{ws}(f)$. Here $E^{ws}(f)$ is estimated using a 1D wave spectral partitioning technique following *Portilla et al.* [2009]. The solid lines in Figure A.2d represent the T_m and T_p values predicted by the Pierson-Moskowitz spectrum, a representative spectrum of fully developed wind-driven seas.

Figure A.2e shows the observed range of several characteristic wave heights as a function of U_{10N}, with $H_s = 4(\int E(f) df)^{1/2}$ the total significant wave height, $H_p = 4(\int_{0.7 f_p}^{1.3 f_p} E(f) df)^{1/2}$ a peak wave height (after *Banner et al.* [2000]), and $H_s^{ws} = 4(\int E^{ws}(f) df)^{1/2}$ the wind sea significant wave height. Two estimates of the significant wave height of fully developed seas $H_{s,\mathrm{fd}}$ (solid lines) given by *Carter* [1982] and *Chen et al.* [2002] are also plotted in Figure A.2e. Results shown in Figures A.2d and A.2e indicate that significant swell is present at moderate and calm winds in the PAPA data.

Several estimates of the corresponding wave age are presented in Figure A.2f, where c_p and c_m are the wave phase speeds corresponding to f_p and f_m, respectively. These results show that a significant portion of the PAPA data at high winds ($U_{10N} \geq 15$ms^{-1}) are characterized as developing seas ($c_p/u_* < 30$ or $c_p/U_{10N} < 1.2$), and that equilibrium seas ($c_p/u_* \approx 30$ or $c_p/U_{10N} \approx 1.2$) are mostly observed at moderate winds.

It is generally accepted that the wave steepness (or slope), defined as $S = Hk/2$ with H and k are a characteristic wave height and wavenumber, is the most relevant local geometric wave parameter to characterize surface gravity wave breaking and related processes in deep water [*Perlin et al.*, 2013]. Several formulations have been proposed to quantify a representative wave steepness in a wave-averaged sense which are either defined based on wave spectral information [*Banner et al.*, 2002] or bulk wave parameters [*Banner et al.*, 2000].

A measure of mean square slope (mss) over a frequency range $f_1 \le f \le f_2$, as proposed by *Banner et al.* [2002], is calculated as

$$mss = \int_{f_1}^{f_2} k^2 E(f) df = \int_{f_1}^{f_2} \frac{(2\pi f)^4}{g^2} E(f) df, \tag{2}$$

and is shown to be a skillful spectral steepness parameter for predicting wave breaking statistics in the open ocean [*Schwendeman and Thomson*, 2015a; *Brumer et al.*, 2017]. Many field observations of the speed of visible breaking wave crests [*Phillips et al.*, 2001; *Melville and Matusov*, 2002; *Gemmrich et al.*, 2008; *Thomson and Jessup*, 2009; *Kleiss and Melville*, 2010; *Sutherland and Melville*, 2013; *Schwendeman et al.*, 2014] have shown that most of surface gravity wave breaking occurs at frequencies noticeably greater than the frequency at the peak of $E(f)$, f_p, with most frequent breaking occurring at $\approx 2f_p$. We note that f_m/f_p varies between 0.9 and 1.6 in the PAPA data (Figure A.2d) where most of the f_m/f_p values are within a range $(1.1-1.4)$, and that the Pierson-Moskowitz spectrum gives $f_m/f_p \approx 1.30$. Following *Schwendeman and Thomson* [2015a], here we take an equilibrium range mss calculated over a frequency range $\sqrt{2} f_m \le f \le \sqrt{5} f_m$ ($2k_m \le k \le 5k_m$, $c_m/\sqrt{5} \le c \le c_m/\sqrt{2}$), which is related to an average spectral steepness of a significant portion of visible breaking waves, especially in developed and equilibrium sea states.

Figures A.2g and A.2h show the variation of the equilibrium range mss and $mss/\Delta f$ ($\Delta f = (\sqrt{5}-\sqrt{2}) f_m$) against U_{10N}, all colored by wind accelerations dU_{10N}/dt defined as the rate of change of U_{10N} over 1.5 hr, in the PAPA data together with the corresponding data from *Schwendeman and Thomson* [2015a]. Figures A.2g and A.2h also show the corresponding values that are obtained from the Pierson-Moskowitz spectrum, which is a representative spectrum of a fully developed sea under constant wind ($dU_{10N}/dt = 0$), given by $[mss]_{PM} \approx 0.436\alpha$ ($\alpha = 8.1 \times 10^{-3}$) and $[mss/\Delta f]_{PM} \approx \pi \alpha g^{-1} U_{10N}$. Figures A.2g also shows that the observed equilibrium range mss in equilibrium, developing, and old seas are, on average, consistent with, greater, and smaller than those predicted by the Pierson-Moskowitz spectrum, respectively. Further, our observations corroborate the analytical relations obtained from the Pierson-Moskowitz spectrum, i.e., equilibrium range mss is independent of wind speeds and $mss/\Delta f \propto U_{10N}$ in fully developed seas with constant winds. Further, Figure A.2i shows the corresponding wind sea $mss^{ws}/\Delta f$ values where mss^{ws} is calculated as given by Eq. 2 but using $E^{ws}(f)$ over a frequency range $\sqrt{2} f_m \le f \le \sqrt{5} f_m$.

Schwendeman and Thomson [2015a] and *Brumer et al.* [2017] used a normalized mss parameter, $mss/\Delta f \Delta\theta$, where $\Delta\theta$ is the average of $\Delta\theta(f)$ over $\sqrt{2} f_m \le f \le \sqrt{5} f_m$ and reported a decrease of data scatter in their plots of whitecap coverage against $mss/\Delta f \Delta\theta$ compared to mss. At any given wind speed, the $mss/\Delta f \Delta\theta$ values in the present data are, on average, greater than those in *Schwendeman and Thomson* [2015a] despite consistent mss and mss/Δf values in both data sets. We note that $mss/\Delta f \Delta\theta$ can not be defined in a long-crested wavefield or from a 1D wave spectrum. We further note that $\Delta\theta$ is sensitive to the type of buoy and method of processing [*Donelan et al.*, 2015], such that values may not be directly comparable between data sets. Here we avoid the directional normalization and choose the equilibrium range $mss/\Delta f$ as a representative measure of spectral steepness of dominant breaking waves.

The observed range of several bulk steepness parameters, including the significant spectral peak steepness $H_p k_p/2$ (after by *Banner et al.* [2000]) and the significant wave steepness $H_s k_p/2$, against $mss/\Delta f$ are shown in Figures A.2j and A.2k. Here the peak k_p and mean k_m wave numbers are obtained from the linear gravity wave dispersion relation given by $k = (2\pi)^2 g^{-1} T^{-2}$. Consistent with the literature, we consider these bulk steepness parameters here.

Finally, several dimensionless bulk parameters with general forms of

$$R_H = u_* H / \nu_w, \tag{3}$$

and

$$R_B = u_*^2 / (2\pi T^{-1} \nu_w), \tag{4}$$

where $\nu_w \approx 1.4\times10^{-6}$ m^{2}s^{-1} is the kinematic viscosity of seawater for $T_w \approx 9$C°, are considered. These parameters represent combined effects of wind forcing and wave field and are shown to have skills in predicting oceanic whitecap coverage [*Zhao and Toba*, 2001; *Scanlon and Ward*, 2016; *Brumer et al.*, 2017]. Figure A.2l shows the variation of $R_{H_{eq}} = u_* H_{eq}/\nu_w$ and $R_B^m = u_*^2/(2\pi T_m^{-1}\nu_w)$ parameters as a function of the equilibrium range $mss/\Delta f$ in the PAPA data. Here $H_{eq} = 4[\int_{\sqrt{2}f_m}^{\sqrt{5}f_m} E(f)df]^{1/2}$ and $T_m = f_m^{-1}$ are taken as a characteristic wave height H and period T, respectively.

2.4 Whitecap Processing

The whitecap coverage data set in this study is the same as the North Pacific whitecap coverage data set described in the recent study by *Malila et al.* [2022]. This section provides a summary of the acquisition and processing of the data set, much of which is equal or similar in terms of hardware and software to the study by *Schwendeman and Thomson* [2015a].

Visual images of the sea surface were collected from shipboard video camera systems on the port and starboard sides of the vessel. The cameras, of model PointGrey Flea2 equipped with 2.8 mm focal-length lenses, recorded at 5–7.5 frames per second during daylight hours. A total of 60 hours of image data were collected while the ship was stationary, mostly coincident with the SWIFT buoy deployments and recoveries. The video acquisitions varied in length between 5 and 60 minutes, but the final mean whitecap coverage W values were obtained over 10–20-minutes bursts. Each W value represents a 10-minute average of consecutive frames.

The image processing of the grayscale video frames for whitecap coverage estimation followed the approach of *Schwendeman and Thomson* [2015a], in which the ship motion due to waves (i.e., pitch and roll) was corrected for using a slightly modified version of the horizon tracking algorithm of *Schwendeman and Thomson* [2015b]. The stabilized images were subsequently geo-rectified and gridded to regular grids with 0.8 m grid resolution. The whitecap-related foam was isolated from the stabilized, geo-rectified, and gridded frames using the pixel intensity thresholding algorithm of *Kleiss and Melville* [2011]. The frame-wise fractional whitecap coverage was then computed as the ratio of pixels detected as belonging to whitecaps (given a value of one) to the total number of pixels in the frame. A subset of the original and thresholded frames in each burst was visually quality controlled for satisfactory image exposure and lens contamination (e.g., raindrops or sea spray). Only image sequences with consistent lighting conditions and minimal lens contamination were used in the final data set.

2.5 Echogram Processing

Acoustic backscattering data were obtained using the echosounding capabilities of the downward-looking beam of the Nortek Signature1000 acoustic Doppler current profiler (ADCP) mounted on the version 4 SWIFT buoys. During the PAPA cruise manufacturer firmware version 2205 was used. Sampling frequencies and pulse repetition rates for the echosounder were 1 MHz and one second, respectively. A transmit pulse duration of 500 μs was used. The vertical sampling resolution provided by the instrument is 1 cm and is presented to depths from 0.3 m $\leq z_w \leq$ 30.3m, where z_w is positive downward and $z_w = 0$ represents the instantaneous free surface level after accounting for the depth of the unit on the SWIFTs. The echosounder mode was operated in 512-s bursts gathered in the surface-following reference frame, from which echograms are presented. Based on the size of the transducer and the operational frequency, we estimate that the echosounders' acoustic near-field based on the definition provided in *Medwin and Clay* [1998] is less than 1 m. To limit the potential impacts of the acoustic near-field, we present data only from ranges greater than 1 m from the transducer face (i.e., depth range from 1.3 m $\leq z_w \leq$ 30.3m).

As detailed below, penetration depths of bubble plumes are estimated from the volume backscattering strength. The volume backscattering strength S_v [dB re 1m^{-1}] is the logarithmic form of the backscattering cross section per unit volume M_v as is given by [*Vagle et al.*, 2012]. When the signal is dominated by the presence of bubbles, as is the focus on this manuscript, this is described by

$$\begin{aligned} S_v =& 10\log_{10} M_v = 10\log_{10}\int_0^\infty \sigma_s(a_b)N(a_b)da_b \\ =& 10\log_{10}(10^{\frac{Pr}{10}} - 10^{\frac{Nt}{10}}) + 20\log_{10} r + 2\alpha r + G_{cal} - 10\log_{10}(\frac{c\tau}{2}) - \phi, \end{aligned} \tag{5}$$

where $\sigma_s(a_b) = 4\pi a_b^2/([(f_R/f)^2 - 1]^2 + \delta^2)$ [m^2] is the scattering cross section for a bubble with radius a_b [m] and $N(a_b)$ is the bubble size distribution. The right-hand side of the equation is an implementation of the sonar equation where Pr is the received signal including noise, Nt is the noise threshold, r is the range from the transducer, α is the attenuation coefficient, c is the speed of sound in the water, τ is the transmit pulse duration, ϕ is the equivalent beam angle, and G_{cal} is a gain factor for a configured transmit power level for the transducer (see Appendix A). G_{cal} was determined by using standard calibration techniques for echosounders [*Demer et al.*, 2015]. We note that we identified issues with the saturation of the signals associated with system gains during calibration. This results in saturated signals at short ranges when measured backscattering intensity is high, thereby truncating the dynamic range of the system at the upper end. A longer discussion of this is also included in Appendix A.

To estimate the average noise level of the transducer, we calculate burst-averaged Pr values at large ranges at low sea states at which the measured signal, not compensated for range and attenuation, does not vary with depth. At these ranges, we assume that due to transmission losses and the weak scattering in the water column the system is simply measuring its own electrical noise and that increases in S_v are driven primarily by the addition of the time-varying gain components in Eq. 5. This approach is consistent with those often applied in fisheries acoustics applications (e.g., *De Robertis and Higginbottom* [2007]. Here we found the average noise level of approximately 22 [dB] and set $Nt = 26$ [dB], i.e., only echogram data values with $Pr > Nt$ are considered for the bubble statistics analysis. We note that subsequent firmware revisions and different internal or internal processing parameters are expected to result in different noise thresholds and calibration gains.

To estimate the local penetration depth of entrained bubbles, we first need to identify a threshold S_v^{th} below which the backscatter signal indicates the absence of signals associated with entrained bubbles exceeding the background conditions. These background conditions may be driven by populations of tiny residual bubbles, biological backscattering, or microstructure in the upper water column. Note that the mixed layer depth was always greater than 40 m in areas sampled during the PAPA cruise; thus, acoustic scattering from stratification can be neglected.

The local penetration depth of entrained bubbles is then defined relative to the instantaneous free surface level ($z_w = 0$) at the vertical level Z_b, in the surface-following reference frame, at which $S_v > S_v^{th}$ for $z_w \le Z_b$; otherwise Z_b = NaN (Not-a-Number). We note that this thresholding technique to estimate bubble penetration depth is analogous to the pixel intensity thresholding commonly used for whitecap coverage estimations (see §2.4). Similar thresholding techniques have been used by previous studies [*Thorpe*, 1986; *Dahl and Jessup*, 1995; *Trevorrow*, 2003; *Vagle et al.*, 2010; *Wang et al.*, 2016] with empirical S_v^{th} values ranging from -70 dB re 1/m to -50 dB re 1/m using sonars with operating frequencies ranging between ≈ 20kHz and ≈ 200kHz. Hereafter we refer to this bubble detection method as BDM1.

We identified the time between 18:00 and 19:00 UTC Dec 16 as a period with relatively calm sea surface conditions and minimal whitecapping during which no visible bubbles and surface foam were observed in the above-surface, and sub-surface images collected by the cameras integrated on SWIFT buoys along with the images from the shipboard cameras. Further, Figure A.1b shows that the wind speeds just before the SWIFTs deployment on Dec 16 were less than 3 ms^{-1} for several hours. Figure A.1b also shows that although wind speed was increasing during the rest of the day in the presence of steady rain, it remained below 5 ms^{-1} between 18:00 and 19:00 UTC. These observations suggest this is a suitable period for establishing baseline levels for near-surface backscattering with negligible contributions of bubbles injected by active breaking at the surface.

The baseline can be established by using statistical averages of the S_v from this relatively calm period with low levels of observed volume backscattering. Figure A.3a shows an example echogram, above-surface image, and vertical profiles of burst-averaged and top 10%-averaged of S_v values just after the low backscattering conditions on Dec 16 described above. The echogram data during low-backscattering conditions reveals that significant portions of the corresponding S_v values vary between -90 dB re 1/m and -75 dB re 1/m with the burst-averaged values, $\overline{S}_v$, less than -80 dB re 1/m. We also found that $\overline{S}_v < -80$ dB re 1/m holds for the rest of calm sea state conditions ($U_{10N} < 3$ ms^{-1}, $dU_{10N}/dt < 1$ ms^{-1}) within the PAPA data. We take $S_v^{th} = -70$ dB re 1/m (as in *Vagle et al.* [2010]) to distinguish between regions with and without the presence of recently entrained bubbles in the water column.

Even very low bubble void fractions, $O(10^{-7})$ or less, can result in S_v values greater than S_v^{th} due to the relatively strong acoustic backscattering response of bubbles [*Dahl and Jessup*, 1995], even when they are sampled well above resonance. For reference, at 1 MHz bubble radii from approximately 3 μm to 7 μm would be resonant in the upper water column [*Medwin and Clay*, 1998; *Vagle and Farmer*, 1998]. We assume that these smaller bubbles dissolve rapidly ($<$ 10 seconds), even when the upper water column is supersaturated, as suggested by *Blanchard and Woodcock* [1957]. Thus, the measured backscattering reflects backscattering from an unknown and evolving population of bubbles that are dissolving and slowly transported by their own buoyancy and/or local currents and turbulence.

We define another estimate of the local penetration depth of entrained bubbles as the depth $z_b(\leq Z_b)$ at which $S_v > S_v^{th}$ for $z_w \leq z_b$ and $S_v > S_v^{th}$+20 dB for $z_b/2 \leq z_w \leq z_b$; otherwise z_b = NaN. That is, the penetration depth is defined by the depth at which the volume backscattering signal continuously exceeds the defined threshold at the surface, and S_v values deeper in the water column exceed background thresholds by at least 20 dB. Hereafter we refer to this bubble detection method as BDM2.

Figure A.3 shows examples of echogram data and the corresponding Z_b (obtained from BDM1, dotted-dashed lines) and z_b (obtained from BDM2, solid lines) values during a developing sea on Dec 16 just after the relatively bubble-free condition described above (panels *a* and *b*) and during a storm with sustained wind speeds of greater than 18 ms^{-1} on Dec 11 (panels *c* and *d*). Figure A.3 also shows examples of subsurface optical images, collected at times when $S_v < S_v^{th}$ for 1.3 m $\leq z_w$ (panel *e*), portions of S_v values are greater than S_v^{th} but remain below S_v^{th}+20 dB (panels f and g), and a portion of S_v values is greater than $S_v > S_v^{th} + 20$ (panels h, i and j). These images qualitatively demonstrate that the entrained surface bubbles at times at which both BDM1 and BDM2 are satisfied, i.e., $Z_b \neq$ NaN and $z_b \neq$ NaN, have significantly more subsurface visible optical signature than those at times at which $Z_b \neq$ NaN but z_b = NaN. Comparing all available concurrent subsurface images and echogram data, we conclude that a similar trend exists across all the PAPA data.

Although we cannot ultimately constrain the differences in void fractions or bubble populations using our sampling method, we can confidently state that our second bubble detection criterion (BDM2) laid out above identifies periods where void fractions increase by a minimum of two orders of magnitude compared to the first bubble detection criterion (BDM1). Under the simplest conditions where bubble size distribution remains constant, a 20 dB increase in backscattering would correspond to an increase in the void fraction of two orders of magnitude. This is driven by a linear relationship between backscattering and the number of scatterers so long as the distribution has not changed or has not been attenuated by high bubble volumes. (Eq. 5). Furthermore, the high bubble void fractions following breaking waves may result in significant excess attenuation of the signals, which is not accounted for in our analysis here [*Vagle and Farmer*, 1998; *Deane et al.*, 2016; *Bassett and Lavery*, 2021]. Such observations have been reported at lower frequencies, where extinction cross sections for resonant bubbles are much larger, but we expect that the high void fractions following a breaking event will also have a temporary impact on measured acoustic backscatter. The result of this is that increases in volume backscattering following localized breaking events likely understate the increase in scattering that would otherwise be observed from the bubble populations, given the transducer's location near the surface.

Overall, z_b values represent the local penetration depths of entrained bubbles that have significantly more void fraction and visible optical signature than those that reach Z_b. This is consistent with a broad range of prior observations measuring bubbles in the upper ocean, which show significant decreases in bubble densities with depth [*Vagle and Farmer*, 1998; *Medwin*, 1977].

3 Results

In this section, we present the observations of the residence time (§3.1) and the penetration depth (§3.2) of bubble plumes and whitecap coverage (§3.3) as a function of various wind and sea state parameters defined in §2. Estimations of the volume of bubble plumes from the measured whitecap coverage and plume penetration depths are discussed in the next section.

3.1 Bubble Plume Residence Time

Figure A.4a shows a schematic of a SWIFT track drifting across an intermittent field of saturated (with visible optical surface signature) and diffused (without visible optical surface signature) bubble clouds during a 512-s burst of data along which echogram data are collected in a surface following reference frame. The buoy has a "wind slip" velocity relative to the surface water $U_{slip} \approx 0.01U_{10N}$ that is caused by wind drag on the portion of the buoy above the surface [*Iyer et al.*, 2022]. Note that the example SWIFT track shown here is calculated with respect to the earth frame, so the example includes both the true surface current and the wind slip of the buoy (which combine together to make the observed drift velocity of the buoy, typically $U_{drift} \approx 0.04U_{10N}$). Thus apparent residence time of detectable bubble clouds in echogram data could be shorter than their true residence time due to the relative drift of the buoys.

As illustrated in Figure A.4a, the apparent residence time of each bubble cloud in echogram data is directly related to the way the buoy crosses the bubble cloud with respect to its main axis. To minimize this potential sampling bias, here we define the residence time of bubble plumes as an average of the highest one-third of the apparent residence time of bubble clouds detected in all concurrent bursts of the echogram data.

Figure A.4b shows the variation of the bubble plume residence times T_{bp} and $T_{bp,v}$ scaled by the wind sea mean wave period T_m^{ws} (defined in §2.3) for wind speeds greater than 6 ms^{-1}. Hereafter the statistics of bubble plumes obtained from the bubble detection methods BDM1 and BDM2 (described in §2.5) are denoted by $()_{bp}$ and $()_{bp,v}$, respectively. Results indicate that the bubble plumes, especially those detected by BDM1, persist in the water column much longer than the corresponding dominant active breaking period, which is expected to be a fraction of T_m^{ws}.

Figure A.5 shows the sub-surface visible signature of an example evolving bubble plume at several instances during (panels $(a1)$ to $(a3)$) and after (panels $(a4)$ to $(a8)$) active breaking collected by a GoPro camera on a SWIFT buoy looking from behind (upwave) the breaking event in an old sea with moderate wind speeds of $U_{10N} \approx 11$ ms^{-1} and $T_m^{ws} \approx 6$s. Figure A.6 also shows example sub-surface images of two evolving bubble plumes during (panels $(a-c)$ and $(e-f)$) and after (panels d and $g-h$) active breaking during a storm with sustained wind speeds of $U_{10N} > 18$ ms^{-1} and $T_m^{ws} \approx 10$s. These images qualitatively show that void fractions in the bubble plumes rapidly decrease after the active breaking period and that residual void fractions persist for many wave periods. These observations are consistent with previous experimental [*Lamarre and Melville*, 1991; *Blenkinsopp and Chaplin*, 2007; *Anguelova and Huq*, 2012] and numerical [*Derakhti and Kirby*, 2014, 2016; *Derakhti et al.*, 2018, 2020a,b] studies of laboratory-scale breaking waves showing that average void fractions within bubble clouds vary from $O(10\%)$

to $O(1\%)$ during active breaking, and then, drop rapidly by several orders of magnitude within a few wave periods.

As discussed in detail in §2.5, plume regions with tiny bubble void fractions, e.g., the diffused bubble clouds shown in panels ($a7$) and ($a8$) of Figure A.5, are still detectable in our sampling method. Assuming that the scattering is dominated by bubbles with radii less than 100 μm, the low bubble rise velocities (i.e., a few cms^{-1} or less) would yield bubble residence times of O(minutes) which is consistent with the apparent residence time of the bubble plumes detected by BDM1 (Figure A.4b), here $T_{bp} \approx$ 100s and $\approx$ 200s for sea states similar to Figure A.5 and Figure A.6, respectively. Thus the statistics of the bubble plumes detected by BDM1, referred to by subscript bp, correspond to bubble plumes ranging from saturated plumes during active breaking to highly diffused plumes that may remain in the water column long after active breaking (e.g., panel ($a8$) of Figure A.5). These observations also confirm that the bubble plumes detected by BDM2 in a given sea state represent plumes that have much shorter residence times and much more visible optical signature than those detected by BDM1 but noticeably exceed the persistence of visible surface foam formed during breaking, here $T_{bp,v} \approx$ 12s and $\approx$ 40s for sea states similar to Figure A.5 and Figure A.6, respectively.

3.2 Bubble Plume Penetration Depth

Example sub-surface images of the bubble plume shown in Figure A.5 illustrate that the average plume penetration depth (and volume) rapidly increases during the initial phase of the bubble plume evolution (e.g., panels ($a1$) to ($a5$), over several seconds). As shown in panels ($a6$) to ($a8$), the overall size of the plume keeps increasing for several wave periods but at rates much lower than during active breaking. This is consistent with the evolution of bubble plumes, turbulent kinetic energy (TKE), and dye patches in previous numerical and experimental studies of laboratory-scale isolated breaking focused waves [*Rapp and Melville*, 1990; *Melville et al.*, 2002; *Derakhti and Kirby*, 2014; *Derakhti et al.*, 2018, 2020a]. Large-scale coherent structures generated by wave breaking crests are among potential drivers of such slow but persistent transport of bubbles long after active breaking [*Melville et al.*, 2002; *Derakhti and Kirby*, 2014; *Derakhti et al.*, 2016].

We define the mean, $\overline{D}_{bp}$ and $\overline{D}_{bp,v}$, and significant bubble plume depths, $D_{bp}^{1/3}$ and $D_{bp,v}^{1/3}$, as

$$\overline{D}_{bp} = \frac{\sum_{i=1}^{N_{Z_b}} Z_b^i}{N_{Z_b}}, \quad \overline{D}_{bp,v} = \frac{\sum_{i=1}^{N_{z_b}} z_b^i}{N_{z_b}}, \tag{6}$$

and

$$D_{bp}^{1/3} = \frac{\sum_{i=2N_{Z_b}/3}^{N_{Z_b}} Z_b^i}{N_{Z_b}/3}, \quad D_{bp,v}^{1/3} = \frac{\sum_{i=2N_{z_b}/3}^{N_{z_b}} z_b^i}{N_{z_b}/3}, \tag{7}$$

where 1.3m $\le Z_b^i \le Z_b^{i+1} \le$ 30.3m, 1.3m $\le z_b^i \le z_b^{i+1} \le$ 30.3m (see Figure A.3), and N_{Z_b} and N_{z_b} are the total numbers of the estimated Z_b (obtained from BDM1) and z_b (obtained from BDM2) values over available concurrent (1 to 4) bursts (each burst includes more than 8 minutes of data) of echogram data, respectively. The representative mean and significant bubble plume depths are obtained at 12-minute intervals at which the wind and wave statistics are available.

Figure A.7 shows the variation of the mean (Eq. 6) and significant (Eq. 7) bubble plume depths as a function of wind speed U_{10N} and equilibrium range $mss/\Delta f$ (Eq. 2) and the corresponding best fits. All the plume depth measures are well correlated with wind speed and $mss/\Delta f$ with data scatter smaller than existing whitecap coverage data sets (including the PAPA data set shown in Figure A.11 below). Because time-dependent bubble depths less than 1.3 m are unavailable here, the resultant plume depth statistics are expected to be biased high in low winds. Hereafter the data points with $U_{10N} <$ 6 ms^{-1} are not considered in obtaining the relevant fits and their statistics. (This is also a typical minimum wind speed for visible whitecaps to occur.)

Of the bubble depths defined here (by Eqs. 6 and 7 above), $\overline{D}_{bp}$ is defined similar to previous studies [*Vagle et al.*, 2010; *Wang et al.*, 2016; *Strand et al.*, 2020]. Our observations, shown in Figure A.7a, indicate that the mean bubble plume depth $\overline{D}_{bp}$ could be up to 14 m at $U_{10N} \approx$ 20 ms^{-1}. This is in good agreement with the observations of *Vagle et al.* [2010] and *Strand et al.* [2020].

The black solid line in Figure A.7a represents the best fit to the binned $\overline{D}_{bp}$ values with a power law form given by

$$\overline{D}_{bp} = 0.092\,[U_{10N}]^{1.58} \tag{8}$$

with $r^2 = 0.90$ defined as in Eq. 12 below. As shown in Figure A.7a, the linear fit by *Vagle et al.* [2010] also well describes the observed variability of $\overline{D}_{bp}$ for moderate winds. For high winds, however, the relationship between $\overline{D}_{bp}$ and wind speed becomes nonlinear, and the $\overline{D}_{bp}$ values are, on average, greater than those reported by *Vagle et al.* [2010]. Underprediction of $\overline{D}_{bp}$ at high winds in *Vagle et al.* [2010] could be simply due to the linear extrapolation of S_v at depths greater than 8m (see their Figure 3). *Wang et al.* [2016] also found a nonlinear relationship between mean bubble depth and wind speed at high winds. However, their mean bubble depths are significantly (factor of 1.5-2) higher than the present (and other) observations. We note that the averaging time used to obtain $\overline{D}_{bp}$ at high winds is 8 or 16 minutes (depending on available concurrent bursts) which is comparable to that in *Wang et al.* [2016].

At any given wind speed, individual breaking events could generate bubble clouds with penetration depths much higher than $\overline{D}_{bp}$. For example, Figure A.3c documents an example individual bubble cloud with a penetration depth of $\approx$ 30 m which is approximately three times greater than the corresponding average bubble plume depth (e.g., Eq. 8). Figure A.8 shows that the Rayleigh distribution could reasonably describe the observed probability distribution function (PDF) of the D_{bp} values at various wind speeds, especially for $D_{bp} > \overline{D}_{bp}$. Assuming the Rayleigh distribution for D_{bp}, we obtain the significant bubble depth as $D_{bp}^{1/3} \approx 1.6\overline{D}_{bp}$ which is consistent with our observations especially for $U_{10N} > 10$ ms^{-1}. The best fit to the observed binned $D_{bp}^{1/3}$ values with a power law form (black solid line in Figure A.7c) is obtained as

$$D_{bp}^{1/3} = 0.13[U_{10N}]^{1.63}, \tag{9}$$

with $r^2 = 0.92$. Assuming the Rayleigh distribution for D_{bp}, the maximum bubble depth is further approximated as

$$D_{bp}^{max} \approx 2D_{bp}^{1/3} \approx 3.2\overline{D}_{bp}. \tag{10}$$

As explained in detail in §2.5 and consistent with observations shown in §3.1, at a given sea state condition $D_{bp,v}$ represents penetration depth of bubbles that have, on average, at least two orders of magnitude more void fraction and significantly more visible optical signature than those reach to D_{bp}. Figure A.8 shows that the population of the bubble plume depth $D_{bp,v}$ values around their mean is considerably elevated compared to that in D_{bp} and that the observed PDF of $D_{bp,v}$ is better described by the Gamma distribution. Furthermore, our observations show that $D_{bp,v}^{1/3}/\overline{D}_{bp,v}$ varies, on average, from 1.2 at low winds to 1.5 at high winds, and that, in contrast to $D_{bp}^{1/3}$, $D_{bp,v}^{1/3}$ has an approximately linear relationship with wind speed. As shown in Figure A.7 the ratio $D_{bp,v}^{1/3}/D_{bp}^{1/3}$ decreases with increasing wind speeds, varies from ≈ 1 at low winds to ≈ 0.6 at high winds.

We examine the predictive skill of several wind and wave parameters, commonly used for parameterizations of whitecap coverage, for bubble plume depths $D_{bp}^{1/3}$ and $D_{bp,v}^{1/3}$. We quantify the skill of each predictor $\mathcal{X}$ (e.g., $U_{10N}, u_*, \mathrm{mss}/\Delta f, S, R, \ldots$, all defined in §2) by calculating the best fit with a power law form $a\mathcal{X}^n$ to the binned $D_{bp}^{1/3}$ and $D_{bp,v}^{1/3}$ values, using the least squares method and then comparing the corresponding fit statistics obtained over all individual data points with $U_{10N} \geq 6$ ms^{-1}. Bins containing fewer than four bursts of data are not considered for data fitting. Here we consider the root-mean-square error (RMSE) and the coefficient of determination r^2, which represent the overall quality of the fits, given by

$$\mathrm{RMSE} = \sqrt{\frac{\Sigma_{i=1}^{i=N} D_{res,i}^2}{N}}, \tag{11}$$

and

$$r^2 = 1 - \frac{\Sigma_{i=1}^{i=N} D_{res,i}^2}{\Sigma_{i=1}^{i=N} (D_i - \overline{D_i})^2}, \tag{12}$$

where $D_{res,i} = D_i - [a\,(X_i)^n]$, D_i is either $D_{bp}^{1/3}$ or $D_{bp,v}^{1/3}$, N is the number of observations, and the overbar indicates an average over all the considered data points. Here RMSE, defined in linear space, indicates an average deviation from the fit, and r^2 indicates the proportion of the observed variability of the bubble plume depths that is predictable from the X parameter. The perfect fit corresponds to $RMSE \sim 0$ and $r^2 \sim 1$.

Table 1 summarizes the coefficients (a and n) and statistics (RMSE, r^2) of the best fits, aX^n, to the PAPA data for several predictive parameters X. Of all the parameters considered here, U_{10N} has the highest skill in predicting the observed variability of both $D_{bp}^{1/3}$ and $D_{bp,v}^{1/3}$. Results summarized in Table 1 also document that the equilibrium range $mss/\Delta f$ and $H_s K_m/2$ show the highest skill among the spectral and bulk wave steepness predictors, respectively. For each type of the predictors considered here, those that contain either the peak wave height, peak wave number, or peak wave period show the least skill. These results also hold for the mean bubble plume depths statistics $\overline{D}_{bp}$ and $\overline{D}_{bp,v}$.

Next, we examine how the bubble plume penetration depths, defined in Eqs. 6 and 7 above and shown in Figure A.7, scaled by significant wave height H_s and mean wavelength $L_m = 2\pi/k_m$ vary in various sea states. Our observations indicate that $D_{bp}^{1/3}$ (note that $\overline{D}_{bp} \approx 0.6\,D_{bp}^{1/3}$) varies from $0.4H_s$ to $4.8H_s$ and from $0.01L_m$ to $0.20L_m$ for wind speeds greater than 6 ms^{-1} (Figure A.9). This is in good agreement with the observed range of scaled mean bubble depths reported in previous field observations [*Thorpe*, 1986; *Wang et al.*, 2016; *Strand et al.*, 2020].

Bulk wave statistics H_s and L_m (or H_p and L_p) could be completely uncorrelated with the scales of the corresponding wind sea (and dominant breaking waves) in the presence of proportionally significant swell, e.g., in low and moderate winds ($U_{10N} < 15$ms^{-1}) in the PAPA data set as shown in Figures A.2d and A.2e. Thus we also consider the wind sea significant wave height H_s^{ws} and mean wavelength L_m^{ws} as scaling parameters here. Our data show that $D_{bp}^{1/3}$ varies from $1.4H_s^{ws}$ to $9.2H_s^{ws}$ and from $0.06L_m^{ws}$ to $0.33L_m^{ws}$ for wind speeds greater than 6 ms^{-1} (Figure A.9).

Further, the corresponding binned data indicate that $D_{bp}^{1/3} \approx [2.4\text{–}4.4]H_s^{ws}$, and $\approx [0.11\text{–}0.2]L_m^{ws}$ (with $\overline{D}_{bp} \approx [1.6-2.8]H_s^{ws}$, and $\approx [0.07-0.13]L_m^{ws}$). The observed range of these scaled bubble plume depths is comparable with the scaled penetration depth of TKE and dye patches reported in previous numerical and experimental studies of isolated breaking focused waves [*Rapp and Melville*, 1990; *Melville et al.*, 2002; *Derakhti and Kirby*, 2014; *Derakhti et al.*, 2018, 2020a] while the length scales of these laboratory-scale breaking waves are one to two orders of magnitude smaller than those in the PAPA data sets.

Figures A.9 and A.10 show the dependency of some of the scaled plume depths on wind speed and wave age. We note that other scaled plume depths considered here show, on average, a similar trend with increasing wind speeds and wave age. Our observations indicate that all the scaled bubble plume penetration depths considered here vary non-monotonically with increasing wind speeds. However, they are all, on average, decreasing functions of wave age in developing seas (i.e., $c_p/U_{10N} < 1.2$). In other words, during the early stages of a young sea, i.e., $c_p/U_{10N} \ll 1.2$, bubble plume penetration depth scaled by either significant wave height or mean wavelength is, on average, much (two times or more) larger than those in equilibrium sea states, i.e., $c_p/U_{10N} \approx 1.2$. Previous field observations revealed that the former is dominated by plunging breaking waves *Thorpe* [1992], while the dominant breaker type in the latter is expected to be spilling breaking. Previous numerical and experimental studies of laboratory-scale breaking waves indicate that bubbles (and breaking-generated turbulence) penetrate, on average, deeper in the water column beneath a plunger than a spilling breaker with the same length scale, especially during active breaking [*Rapp and Melville*, 1990; *Melville et al.*, 2002; *Derakhti and Kirby*, 2014; *Derakhti et al.*, 2018, 2020a,b]. Thus the observed dependency of scaled bubble

Table 1: Parameterizations of significant bubble plume depths $D_{bp}^{1/3}$ and $D_{bp,v}^{1/3}$ represented by the best fits with a power law form $a\,X^n$ as a function of several wind and wave parameters X to the binned PAPA data for $U_{10N} \geq 6$ ms^{-1}. The statistics of each fit are also calculated. The fits and their statistics are computed in linear space.

Plume Depth	Predictor X	Results of the best fit $a\,X^n$: a	n	Statistics of the best fit $U_{10N} \geq 6$ ms^{-1}: RMSE	r^2
$D_{bp}^{1/3}$	U_{10N}	1.27×10^{-1}	1.63	1.326	0.921
$D_{bp}^{1/3}$	u_*	1.49×10^{1}	1.14	1.417	0.910
$D_{bp}^{1/3}$	$R_{B,m} = \frac{u_*^2}{\nu_w \omega_m}$	1.07×10^{-2}	0.52	1.502	0.899
$D_{bp}^{1/3}$	$R_{B,p} = \frac{u_*^2}{\nu_w \omega_p}$	1.12×10^{-2}	0.51	1.653	0.877
$D_{bp}^{1/3}$	$R_{H_{eq}} = \frac{u_* H_{eq}}{\nu_w}$	2.56×10^{-3}	0.61	1.894	0.839
$D_{bp}^{1/3}$	$R_{H_s} = \frac{u_* H_s}{\nu_w}$	1.36×10^{-3}	0.60	1.986	0.823
$D_{bp}^{1/3}$	$R_{H_p} = \frac{u_* H_p}{\nu_w}$	2.05×10^{-3}	0.59	2.139	0.794
$D_{bp}^{1/3}$	mss	1.86×10^{4}	1.34	2.893	0.619
$D_{bp}^{1/3}$	$\mathrm{mss}/\Delta f$	7.60×10^{2}	1.32	2.419	0.734
$D_{bp}^{1/3}$	$\mathrm{mss}/\Delta f \Delta\theta$	3.35×10^{2}	1.37	2.911	0.614
$D_{bp}^{1/3}$	$H_p k_p/2$	9.06×10^{1}	0.88	4.055	0.251
$D_{bp}^{1/3}$	$H_s k_p/2$	6.33×10^{1}	0.83	4.027	0.262
$D_{bp}^{1/3}$	$H_{eq} k_m/2$	1.34×10^{4}	2.23	3.017	0.586
$D_{bp}^{1/3}$	$H_p k_m/2$	2.20×10^{3}	2.31	3.211	0.531
$D_{bp}^{1/3}$	$H_s k_m/2$	1.29×10^{3}	2.34	2.888	0.620
$D_{bp,v}^{1/3}$	U_{10N}	3.78×10^{-1}	1.10	1.112	0.822
$D_{bp,v}^{1/3}$	u_*	9.55×10^{0}	0.83	1.110	0.822
$D_{bp,v}^{1/3}$	$R_{B,m} = \frac{u_*^2}{\nu_w \omega_m}$	5.09×10^{-2}	0.38	1.139	0.813
$D_{bp,v}^{1/3}$	$R_{B,p} = \frac{u_*^2}{\nu_w \omega_p}$	4.88×10^{-2}	0.37	1.197	0.794
$D_{bp,v}^{1/3}$	$R_{H_{eq}} = \frac{u_* H_{eq}}{\nu_w}$	1.58×10^{-2}	0.45	1.290	0.760
$D_{bp,v}^{1/3}$	$R_{H_s} = \frac{u_* H_s}{\nu_w}$	9.56×10^{-3}	0.45	1.318	0.750
$D_{bp,v}^{1/3}$	$R_{H_p} = \frac{u_* H_p}{\nu_w}$	1.43×10^{-2}	0.43	1.383	0.725
$D_{bp,v}^{1/3}$	mss	1.43×10^{3}	0.94	1.917	0.466
$D_{bp,v}^{1/3}$	$\mathrm{mss}/\Delta f$	1.55×10^{2}	0.94	1.589	0.634
$D_{bp,v}^{1/3}$	$\mathrm{mss}/\Delta f \Delta\theta$	8.62×10^{1}	0.96	1.839	0.509
$D_{bp,v}^{1/3}$	$H_p k_p/2$	2.63×10^{1}	0.50	2.334	0.209
$D_{bp,v}^{1/3}$	$H_s k_p/2$	2.11×10^{1}	0.46	2.341	0.205
$D_{bp,v}^{1/3}$	$H_{eq} k_m/2$	1.25×10^{3}	1.59	1.974	0.434
$D_{bp,v}^{1/3}$	$H_p k_m/2$	2.09×10^{2}	1.44	2.000	0.419
$D_{bp,v}^{1/3}$	$H_s k_m/2$	2.15×10^{2}	1.63	1.858	0.499

plume penetration depths with wave age in developing seas (i.e., $c_p/U_{10N} \approx 1.2$), shown in Figure A.10, is linked to the change in the dominant breaker type.

Further, our results show that the bubble plume penetration depths scaled by either H_s or L_m decrease monotonically with increasing wave age over the observed range of sea states in the PAPA data set from developing to old seas. In particular, the data indicate that $D_{bp}^{1/3}/H_s$ has a linear relationship with the inverse of wave age, given by

$$\frac{D_{bp}^{1/3}}{H_s} = 2.42[\frac{c_p}{U_{10N}}]^{-0.96}, \tag{13}$$

with relatively small data scatter and $r^2 = 0.77$ (solid line in Figure A.10a). Assuming an approximately linear relationship between U_{10N} and air friction velocity (Figure A.2b), the results shown in Figures A.10a and A.10b and Eq. 13 are consistent with the corresponding results reported in *Wang et al.* [2016].

3.3 Whitecap Coverage and Its Relation with Bubble Plume Depths

Existing parameterizations of oceanic whitecap coverage W have a general threshold power law form of $W = a\,(\mathcal{X}-b)^n$, where $\mathcal{X}$ is a selected predictive parameter (e.g., $U_{10N}, u_*, \mathrm{mss}/\Delta f, S, R, \ldots,$ all defined in §2) and a, b and n are empirical coefficients obtained from the best fit to a considered data set by minimizing the sum of the squares of the log residuals $W_{res} = \log_{10} W - \log_{10}[a\,(\mathcal{X} - b)^n]$ to give equal weight to W data across several orders of magnitude. It is generally accepted that several environmental conditions, including surfactants, salinity, wind fetch and duration, wind history, surface shear, and rain, are responsible for data scatter in whitecap variability against a typical predictive parameter $\mathcal{X}$. However, these secondary effects on the corresponding mean W values are thought to be relatively small. Thus, we obtain the corresponding best fits over the binned data as in §3.2 and similar to *Scanlon and Ward* [2016] and *Brumer et al.* [2017]. Bins containing fewer than four bursts of data are not considered for data fitting as in §3.2.

Figures A.11a and A.11b show the variation of W against wind speed and air friction velocity in the PAPA data and in the data set of *Schwendeman and Thomson* [2015a] as well as the best fits to the binned PAPA data and several relevant least squares threshold power law fits from the recent literature [*Sugihara et al.*, 2007; *Callaghan et al.*, 2008; *Schwendeman and Thomson*, 2015a; *Scanlon and Ward*, 2016; *Brumer et al.*, 2017]. Consistent with the recent literature, the observed $W(U_{10N})$ values are considerably smaller than those reported in pioneering W studies [e.g., *Monahan and Muircheartaigh*, 1980] using a manual W extraction method [*Monahan*, 1969]. Further, the observed range of $W(U_{10N})$ and $W(u_*)$ values and their associated data scatter are consistent with the recent studies in which their experimental methods are comparable to those used here (see §2.4).

Figure A.11a shows that the observed $W(U_{10N})$ values and their corresponding best fits at high winds are considerably comparable with those in the other data sets, especially those that include W observations at $U_{10N} > 16$ ms^{-1}; the solid line section of each fit shown in Figure A.11 represents the range of data to which the best fit is obtained. The fits, however, tend to diverge for $U_{10N} < 10$ ms^{-1}. We note that the shape of a threshold power law fit at low and moderate winds and, in particular, the coefficient b (which incorporates the threshold behavior of the fit) are sensitive to the data at the lower range of $\mathcal{X}$ values. Thus, any systematic bias at the selected wind parameter at low wind speeds will be translated into the resulting best fit. Wind speeds in several previous studies were not corrected for atmospheric stability, e.g., *Sugihara et al.* [2007] and *Schwendeman and Thomson* [2015a], or U_{10}^{PL} was simply used as a proxy for U_{10N}, e.g., *Callaghan et al.* [2008]. As discussed in §2.2, although these simplifications have a relatively small effect on estimated wind speeds at high winds, they can lead to considerable errors in estimated wind parameters at low winds.

Our observations shown in Figures A.11a and A.11b demonstrate that the observed $W(U_{10N})$ and $W(u_*)$ values at rapidly decreasing ($dU_{10N}/dt \ll 0$), low winds ($U_{10N} < 4$ ms^{-1} or $u_* <$

0.2 ms^{-1}) vary between 10^{-4} and 2×10^{-3} while the best wind-speed-only or u_*-only fits obtained from the remaining of the data points predict no whitecapping ($W = 0$) at those wind conditions. This suggests that strong wind history could also result in a systematic bias in $W(U_{10N})$ and $W(u_*)$ data at low winds, and thus, may be responsible for a portion of an apparent divergence in existing wind-speed-only and u_*-only fits at low and moderate winds.

Figures A.11a and A.11b also show that at the same wind forcing, either represented by U_{10N} or u_*, a large portion of W values in the PAPA data at increasing ($dU_{10N}/dt > 0$) and decreasing ($dU_{10N}/dt < 0$) wind speeds tend to be smaller and greater than the corresponding mean W values provided by the corresponding best fits, respectively. This trend is consistent with the observations of *Callaghan et al.* [2008] for wind speeds above approximately 9 ms^{-1}. However, in contrast to *Callaghan et al.* [2008], our observations clearly show that the same trend exists for moderate and low winds if the magnitude of dU_{10N}/dt is sufficiently large.

Next, we examine the predictive skill of several wind and wave parameters for the observed range of W values in the PAPA data similar to the method described in §3.2 but in $\log_{10}$ space; i.e., we evaluate the overall quality of the fits using Eqs. 11 and 12 with $W_{res,i} = \log_{10} W_i - \log_{10}[a\,(X_i - b)^n]$. Here RMSE indicates an average order of magnitude deviation from the fit, and r^2 indicates the proportion of the observed $\log_{10} W$ variability that is predictable from the X parameter. Negative r^2 indicates that the fit performs worse than a horizontal line at the mean of the data. As in §3.2, all the fits are obtained from the binned data for $U_{10N} \geq 6$ ms^{-1}. The fit statistics are obtained using the individual 10-minute average data points, W_i ($i = 1, \ldots, N$), with three conditions: all data ($N = 165$), $U_{10N} \geq 6$ ms^{-1} ($N = 144$), and $|dU_{10N}/dt| < 2$ ms^{-1}hr^{-1} ($N = 126$).

Table 2: Parameterizations of whitecap coverage represented by the best fits with a threshold power law form $W = a\,(X - b)^n$ as a function of several wind and wave parameters X to the binned PAPA data for $U_{10N} \geq 6$ ms^{-1}. The statistics of each fit are also calculated for three conditions. The fits and their statistics are computed in log space.

Predictor	Results of the best fit			Statistics of the best fit with conditions:					
	$W = a\,(X - b)^n$			$U_{10N} \geq 6$ ms^{-1}		$\lvert\frac{dU_{10N}}{dt}\rvert < 2\ \frac{\text{ms}^{-1}}{\text{hr}}$		all data	
X	a	b	n	RMSE	r^2	RMSE	r^2	RMSE	r^2
U_{10N}	2.06×10^{-5}	3.89	2.65	0.412	0.70	0.471	0.60	0.752	0.05
u_*	3.63×10^{-2}	0.18	2.00	0.394	0.72	0.476	0.59	0.698	0.18
$R_{B,m} = \frac{u_*^2}{\nu_w\,\omega_m}$	3.87×10^{-9}	5.81×10^{4}	1.14	0.400	0.72	0.646	0.25	0.935	−0.47
$R_{B,p} = \frac{u_*^2}{\nu_w\,\omega_p}$	3.86×10^{-9}	7.01×10^{4}	1.12	0.424	0.68	0.657	0.22	0.916	−0.41
$R_{H_{eq}} = \frac{u_* H_{eq}}{\nu_w}$	3.02×10^{-10}	1.50×10^{5}	1.31	0.428	0.68	0.415	0.69	0.645	0.30
$R_{H_s} = \frac{u_* H_s}{\nu_w}$	2.45×10^{-10}	5.07×10^{5}	1.23	0.456	0.63	0.434	0.66	0.692	0.20
$R_{H_p} = \frac{u_* H_p}{\nu_w}$	1.64×10^{-9}	4.05×10^{5}	1.12	0.590	0.38	0.589	0.37	0.801	−0.08
mss	6.50×10^{6}	–	3.60	0.565	0.43	0.557	0.44	0.572	0.44
$\text{mss}/\Delta f$	1.61×10^{2}	6.23×10^{-3}	2.79	0.487	0.58	0.482	0.58	0.512	0.55
$\text{mss}/\Delta f\Delta\theta$	4.79	1.72×10^{-2}	2.16	0.537	0.49	0.534	0.49	0.557	0.47
$H_p k_p/2$	4.85	–	2.33	0.737	0.03	0.520	0.06	0.778	−0.04
$H_s k_p/2$	2.06×10^{-1}	3.86×10^{-2}	0.99	0.766	−0.05	0.795	−0.14	0.837	−0.20
$H_{eq} k_m/2$	1.89×10^{7}	–	6.58	0.564	0.43	0.550	0.46	0.576	0.43
$H_p k_m/2$	3.80×10^{2}	3.12×10^{-2}	3.87	0.547	0.46	0.550	0.46	0.552	0.48
$H_s k_m/2$	5.53×10^{2}	4.56×10^{-2}	4.27	0.507	0.54	0.502	0.54	0.503	0.56

Table 2 summarizes the coefficients (a, b, and n) and statistics of the best fits, $W = a\,(\mathcal{X} - b)^n$, for several predictive parameters $\mathcal{X}$ to the PAPA data. Of all the considered predictors for W at moderate and high winds, u_* gives the best fit ($r^2 = 0.72$, RMSE = 0.394), which is only slightly better than the U_{10N} fit ($r^2 = 0.70$, RMSE = 0.412). Our results show that the quality of the fits obtained from various forms of the predictors R_H (Eq. 3) and R_B (Eq. 4), which combine u_* and a characteristic scale of the wave field, are similar or less than the u_*-only fit. These parameterizations cannot reasonably predict W at rapidly varying wind speeds (i.e., large wind accelerations).

Our observations shown in Figure A.2 indicate that either the normalized or unnormalized equilibrium range mss values at increasing winds are smaller than those in decreasing winds at a given wind speed. This suggests that these spectral parameters might reflect both wind forcing and wind history effects. Consistently, the results summarized in Table 2 document that the parameterizations based on the equilibrium range mss have similar skill across all sea state conditions, including those with large wind accelerations. The results indicate that the equilibrium range $mss/\Delta f$ (Figure A.11c) better predicts the observed W variability compared to the other spectral predictors considered here. Of the bulk steepness predictors, $H_s k_m/2$ has the highest skill. Overall, for each type of the predictors considered here, those that contain either the peak wave height, peak wave number, or peak wave period show the least skill (Figure A.11d).

Figure A.11 shows that the observed $W(U_{10N})$, $W(u_*)$, and $W(mss/\Delta f)$ values in the PAPA data at moderate winds (e.g., 8 ms^{-1} $\leq U_{10N} \leq$ 16 ms^{-1}) are generally smaller than in the *Schwendeman and Thomson* [2015a] data set. We note that a significant portion of the data at these wind speeds was collected in the presence of rain (Figure A.1b). This observation may suggest that whitecap activity is suppressed in the presence of rain. Detailed quantification of rain effects on W requires rain rates (not measured here) and remains unknown.

Finally, Figure A.12 shows that the mean and significant bubble plume penetration depths are, on average, correlated and have a nonlinear relation with whitecap coverage given by

$$\overline{D}_{bp} = 29.5\, W^{0.33}\ ,\quad D_{bp}^{1/3} = 52.8\, W^{0.36}, \tag{14}$$

with $r^2 = 0.60$ (the fit in Figure A.12a) and $r^2 = 0.62$ (the fit in Figure A.12c), and

$$\overline{D}_{bp,v} = 12.6\, W^{0.19}\ ,\quad D_{bp,v}^{1/3} = 21.9\, W^{0.24}, \tag{15}$$

with $r^2 = 0.33$ (the fit in Figure A.12b) and $r^2 = 0.43$ (the fit in Figure A.12d). Here both fits are obtained using the binned data as a function of U_{10N}; as before, the data with $U_{10N} <$ 6ms^{-1} are not considered for data fitting. As explained in detail in §2.5 and consistent with the observations shown in §3.1 and §3.2, $D_{bp,v}$ represents penetration depth of bubbles that have, on average, at least two orders of magnitude more void fraction and significantly more visible optical signature than those reach to D_{bp} for a given sea state condition.

Assuming a wave field with narrow-banded breaking waves, W increases approximately linearly with increasing rates of breaking waves while the statistics of bubble plume depths are not sensitive to breaking rates, and thus they would not be correlated with W. However, wave breaking typically occurs at a range of scales, and increasing W results from increasing both the rate and scale of breaking waves. This may partially explain the observed relationship between bubble plume depths and W shown in Figure A.12, that is, the plume depths increase, on average, with increasing W but at a much lower rate, i.e., the exponents in Eqs. 14 and 15 are positive but much less than 1.

4 Discussion: Bubble Plumes Volumes

Here we define the volume of bubble plumes as a measure of their overall size rather than the total volume of bubbles they contain, with the bubble plumes that are identified as regions in which volume backscattering strength (somewhat related to bubble void fractions, see §2.5) is above a threshold value. That said, the volume of bubble plumes per unit sea surface area is given by

$$\mathcal{V}_{bp} = \mathcal{A}_{bp}\overline{D}_{bp}, \quad \text{and} \quad \mathcal{V}_{bp,v} = \mathcal{A}_{bp,v}\overline{D}_{bp,v}, \tag{16}$$

where $\mathcal{A}$ is the fractional surface area of bubble plumes, $\overline{D}$ is the mean penetration depth of bubbles within the plumes, and the subscripts bp and bp, v denote the statistics corresponding the bubble plumes obtained from our bubble detection methods BDM1 and BDM2 (described in §2.5), respectively. As discussed in detail in §2.5, $\overline{D}_{bp,v}$ represents mean penetration depth of bubbles where the volume backscattering is at least 20 dB higher at $\overline{D}_{bp}$ for a given sea state condition and note this is expected to reflect comparable increasing in void fraction. Our observations and several simple parameterizations of the mean plume depths $\overline{D}_{bp}$ and $\overline{D}_{bp,v}$ are presented in §3.

We note that $\mathcal{A}$ represents the fractional surface area, with or without visible surface signature, of bubble plumes that significantly exceed the persistence of visible surface foam generated during active breaking as discussed in §3.1. Thus both $\mathcal{A}_{bp}$ and $\mathcal{A}_{bp,v}$ are expected to be noticeably greater than the measured whitecap coverage W. However, $\mathcal{A}_{bp}$ and $\mathcal{A}_{bp,v}$ can not be directly quantified from our sampling method. In the following, we introduce a proxy for $\mathcal{A}$ and comment on its relation to W.

We define P as a time fraction of echogram data over concurrent bursts during which bubble plumes are detected. Assuming the buoys had an approximately constant "wind slip" velocity U_{slip} during each burst, $A = P^2$ then provides a proxy for $\mathcal{A}$ if the drifting distance of the buoy relative to the surface water $\approx U_{slip}T_{burst}$ is much greater than the average horizontal length of the bubble clouds $\approx U_{slip}T_{ab}$ or $U_{slip}T_{ab,v}$ (see §3.1). Further, at least a few bubble clouds should be available in a burst to consider that $\mathcal{A} \approx A$.

Figure A.13a shows the A_{bp} and $A_{bp,v}$ values as a function of U_{10N} where the size of the symbols is a function of the number of the bubble clouds detected in a burst, averaged over concurrent bursts, N, with $0.67 \le N_{bp} \le 26$ and $0.5 \le N_{bp,v} \le 24$. Note that P, and thus $A = P^2$, values that approach one indicate that either the main portion of the surface layer is covered by bubble plumes or the net drifting distance of the buoy (relative to the surface water) is smaller than the horizontal length of the sampled bubble cloud. As shown in Figure A.4b and A.13a, the latter may explain $A_{bp} \sim 1$ at moderate winds where $N < 2$ and T_{ab} values are on the order of several hundreds of seconds (comparable to $T_{burst} = 512$s). Despite the uncertainties in the interpretation of A, the observations shown in Figure A.13a suggest that A_{bp} is several times greater than $A_{bp,v}$, which is qualitatively consistent with the continuous increase of the overall size of the bubble plume shown in Figure A.5 and the corresponding residence time results shown in Figure A.4b.

Figure A.13b shows that both A_{bp} and $A_{bp,v}$ are, on average, increase as a function of W as

$$A_{bp} = 2.5\,W^{0.33} \le 1, \quad \text{and} \quad A_{bp,v} = 8.4\,W^{0.97} \le 1. \tag{17}$$

Note that the data points with $N < 3$ are neglected in Figure A.13b. Our observations show that A_{bp}, which is comparable to a fractional surface area defined in *Thorpe* [1986], is at least an order of magnitude larger than W. This is consistent with the semi-empirical plume area analysis of *Thorpe* [1986].

Finally by substituting Eqs. 14, 15, and 17 into Eq. 16, we obtain

$$\mathcal{V}_{bp} = \mathcal{A}_{bp}\overline{D}_{bp} \approx 74\,W^{0.66} \le 29.5\,W^{0.33} \quad [\mathrm{m}^3/\mathrm{m}^2], \tag{18}$$

and

$$\mathcal{V}_{bp,v} = \mathcal{A}_{bp,v}\overline{D}_{bp,v} \approx 106\,W^{1.16} \le 12.6\,W^{0.19} \quad [\mathrm{m}^3/\mathrm{m}^2], \tag{19}$$

assuming that the best fits to the binned data shown in Figure A.13b (Eq. 17) provide a proxy for $\mathcal{A}_{bp}$ and $\mathcal{A}_{bp,v}$.

We emphasize that uncertainty in our estimates of the fractional surface area of bubble plumes (and thus plume volumes) increases with decreasing W, especially at low W values (e.g., $W <$

10^{-3}) because of increasing effect of sparse sampling of intermittent breaking crests on the resulting statistics [*Derakhti et al.*, 2020a].

5 Summary

The observational results presented here quantify the statistics of penetration depth and fractional surface area of bubble plumes generated by breaking surface waves as a function of various wind and sea state parameters over a wide range of sea state conditions. Bubble plume data include concurrent high-resolution (with a 12 min temporal resolution) plume depth statistics and whitecap coverage. The former is obtained from the echogram data with 1 cm vertical resolution, collected by downward-looking echosounders mounted on arrays of freely drifting SWIFT buoys. The latter is obtained from visual images, collected by shipboard cameras operated near the buoys.

Our observations indicate that the statistics of bubble plume penetration depths are well-correlated with wind speed, spectral wave steepness, and whitecap coverage. Results show that the mean plume depths exceed 10 m beneath the surface at high winds, with individual bubble clouds reach to depths of more than 30 m. Mean plume depths vary, on average, from 1.6 to 2.8 times wind sea significant wave height H_s^{ws}. Plume depths scaled by either H_s^{ws} or total significant wave height H_s vary non-monotonically with increasing wind speeds. Plume depths scaled by H_s are strongly linearly correlated with the inverse of wave age from developing to old seas. All scaled plume depths considered here are decreasing functions of wave age in developing seas. We successfully provide multiple parameterizations that predict the observed variability of the penetration depth and surface area of bubble plumes as a function of simple wind and wave statistics available from existing forecast models or typical ocean buoys.

This study is the first to provide a direct relation between bubble plume penetration depth and whitecap coverage, indicating that the penetration depth of bubble plumes is correlated with their visible surface area. This result is significant as it advocates the possibility of estimating the volume of bubble plumes by remote sensing. This also significantly expands the applicability of the recent theoretical framework introduced by *Callaghan* [2018] on predicting total wave breaking dissipation as a function of bubble plume penetration depth and whitecap coverage. In a companion paper, we examine dynamic relationships between the bubble plume statistics presented here and total wave breaking dissipation using our synchronized observations of bubble plumes and dissipation rates.

Finally, the parameterizations of bubble plume penetration depth provided in this study may also be used for estimating effective vertical transport of other particles, with a rising velocity on the order of few cms^{-1} or less, by breaking surface waves. It is possible that the drifting SWIFT buoys used in this study aggregate in convergence zones with enhanced downwelling velocities, such that there would be a sampling bias in the interpretation of vertical transport [*Zippel et al.*, 2020]. However, no obvious convergence zones, windrows, or other organized surface fronts were observed during the PAPA data collection. Furthermore, the wind slip (1% of wind speed) of the buoys tends to cause a quasi-uniform sampling along a drift track even in the presence of surface features.

Open Research

SWIFT data are available from www.apl.washington.edu/swift, and whitecap coverage data are available from http://hdl.handle.net/1773/48143.

Acknowledgments

This work was supported by grants OCE-1756040 and OCE-1756355 from the US National Science Foundation. Sven Nylund from Nortek provided excellent support in processing the echosounder data. The captain and crew of the R/V Sikuliaq provided excellent support at sea during data collection. Joe Talbert and Alex de Klerk built and maintained the SWIFT buoys. Christine Baker, Alex Fisher, Andy Jessup, and Helen Zhang also helped with data collection.

A: Echosounder calibration

The echosounder was calibrated using standard sphere calibration techniques *Demer et al.* [2015]. In this approach, a sphere of a known material is suspended below the beam of an echosounder. Since the sphere's properties are known, an analytical solution for the acoustic target strength can be calculated. The difference between the measured intensity of the scattering and the known scattering from the sphere at the transmit frequency is the total gain for the system. In post-cruise testing, a 38.1 mm diameter tungsten-carbide sphere with 6% cobalt binder was suspended 8 m below the transducers by a bridle connected to the hull of the SWIFTs. The units were then deployed for 30-60 minutes on Lake Washington (Washington, USA), during which the attitude of the SWIFTS caused the suspended sphere to pass through the beam of the echosounder. The top 1% of targets at the sphere range, which are assumed to be those associated with the sphere being on-axis within the beam where the combined transmit-receive beampattern is highest, were then selected. The gain is then determined by solving for G_{cal} in the target strength equation using the known analytical solution for the target strength of the sphere.

In practice, a sphere is sized such that its scattering response contains no significant nulls within the bandwidth [*Demer et al.*, 2015; *Stanton and Chu*, 2008; *Lavery et al.*, 2017]. However, this is not feasible at 1 MHz since a tiny $< 1cm$ sphere would be required. Furthermore, for such a small sphere, the strands securing the sphere would contribute significantly to scattering, bias the results [*Renfree et al.*, 2020]. Thus, we chose to use a larger sphere whose response is quite complex over the relevant frequency range. The pulse-compressed signal has sufficient bandwidth to clearly resolve the echo from the front interface and subsequent contributions from circumference waves. We, therefore, assumed that the peak of the pulse compressed signal represents the partial wave scattering cross-section of the sphere [*Stanton and Chu*, 2008]. This assumption is necessary given that a frequency-dependent calibration cannot be performed given the only output data product is a scattering intensity measurement representing the average within the range bin output by the ADCP.

At the time of this experiment, the firmware resulted in scattering that saturated the receiver in the high gain setting and saturated the receiver when using the calibration sphere at a range of ~8 m. There is, therefore, some uncertainty in the calibration gains and the field observations. We cannot conclusively state the magnitude of this uncertainty, but it is believed to be on the order of a few dB or less from the calibration gain. The justification for this statement is that the elastic response of the sphere is well resolved with the intensity (impulse response squared) of the signal from the first Rayleigh wave, approximately 9 dB smaller than the echo from the front interface of the sphere when the calibrations were performed at the lower gain setting. This is consistent with expectations based on the impulse response of a 38.1 mm tungsten carbine sphere [*Demer et al.*, 2015] and the arrival of the signal associated with the first Rayleigh wave. In the saturated data, the difference in intensity between the first Rayleigh wave and the saturated echo from the front interface was approximately 3 dB. Given the impulse response of the 38.1 mm sphere, this suggests that about 6 dB of scattering from the sphere had been clipped. When used in the high power setting, gains were applied assuming the clipped value was 6 dB. The practical effect of this uncertainty is to put consistent error bars on the volume scattering coefficients measured in the data. That is, all data are shifted similarly, making the absolute intensity of the backscattering more uncertain without impacting the relevant ranges between the thresholds.

The fact that scattering from the tungsten carbide sphere saturated at 8 m indicates the high gain setting almost certainly caused widespread saturation of signals in the upper portion (~ 10 m) of the water column when high densities of bubbles were present. A consequence of this is that the full dynamic range of volume backscattering is not resolved. Despite these challenges and uncertainties, we consider it preferable to present backscattering intensities in this approach to backscattering intensities expressed in decibels with reference value ground in physical measurements.

References

Al-Lashi, R. S., S. R. Gunn, and H. Czerski (2016), Automated processing of oceanic bubble images for measuring bubble size distributions underneath breaking waves, *J. Atmos. Oceanic Tech.*, *33*, doi:10.1175/JTECH-D-15-0222.1.

Anguelova, M. D., and P. Huq (2012), Characteristics of bubble clouds at various wind speeds, *J. Geophys. Res.: Oceans*, *117*, doi:10.1029/2011JC007442.

Banner, M., J. Gemmrich, and D. Farmer (2002), Multiscale measurements of ocean wave breaking probability, *J. Phys. Oceanogr.*, *32*, 3364–3375, doi:10.1175/1520-0485(2002)032⟨3364:MMOOWB⟩2.0.CO;2.

Banner, M. L., A. V. Babanin, and I. Young (2000), Breaking probability for dominant waves on the sea surface, *J. Phys. Oceanogr.*, *30*, 3145–3160, doi:10.1175/1520-0485(2000)030⟨3145:BPFDWO⟩2.0.CO;2.

Bassett, C., and A. Lavery (2021), Observations of high-frequency acoustic attenuation due to bubble entrainment at estuarine fronts, *Proceedings of Meetings on Acoustics*, *45*(1), 005,001, doi:10.1121/2.0001539.

Blanchard, D. C., and A. H. Woodcock (1957), Bubble formation and modification in the sea and its meteorological significance, *Tellus*, *9*(2), 145–158, doi:10.3402/tellusa.v9i2.9094.

Blenkinsopp, C. E., and J. R. Chaplin (2007), Void fraction measurements in breaking waves, *Proc. Royal Soc. A: Math, Phys. Eng. Sci.*, *463*, 3151–3170, doi:10.1098/rspa.2007.1901.

Brumer, S. E., C. J. Zappa, I. M. Brooks, H. Tamura, S. M. Brown, B. W. Blomquist, C. W. Fairall, and A. Cifuentes-Lorenzen (2017), Whitecap coverage dependence on wind and wave statistics as observed during so gasex and hiwings, *J Phys. Oceanogr.*, *47*, 2211–2235, doi:10.1175/JPO-D-17-0005.1.

Callaghan, A., G. de Leeuw, L. Cohen, and C. D. O'Dowd (2008), Relationship of oceanic whitecap coverage to wind speed and wind history, *Geophys. Res. Lett.*, *35*(23), doi:10.1029/2008GL036165.

Callaghan, A. H. (2018), On the relationship between the energy dissipation rate of surface-breaking waves and oceanic whitecap coverage, *J. Phys. Oceanogr.*, *48*, 2609–2626, doi:10.1175/JPO-D-17-0124.1.

Callaghan, A. H., G. B. Deane, and M. D. Stokes (2016), Laboratory air-entraining breaking waves: Imaging visible foam signatures to estimate energy dissipation, *Geophys. Res. Let.*, *43*, 11–320, doi:10.1002/2016GL071226.

Carter, D. (1982), Prediction of wave height and period for a constant wind velocity using the jonswap results, *Ocean Eng.*, *9*, 17–33, doi:10.1016/0029-8018(82)90042-7.

Chen, G., B. Chapron, R. Ezraty, and D. Vandemark (2002), A global view of swell and wind sea climate in the ocean by satellite altimeter and scatterometer, *J. Atm. and Oceanic Tech.*, *19*, 1849–1859, doi:10.1175/1520-0426(2002)019⟨1849:AGVOSA⟩2.0.CO;2.

Dahl, P. H., and A. T. Jessup (1995), On bubble clouds produced by breaking waves: An event analysis of ocean acoustic measurements, *J. Geophys. Res.: Oceans*, *100*, 5007–5020, doi:10.1029/94JC03019.

De Robertis, A., and I. Higginbottom (2007), A post-processing technique to estimate the signal-to-noise ratio and remove echosounder background noise, *ICES J. Mar. Sci.*, *64*(6), 1282–1291, doi:10.1093/icesjms/fsm112.

Deane, G. B., M. D. Stokes, and A. H. Callaghan (2016), The saturation of fluid turbulence in breaking laboratory waves and implications for whitecaps, *J. Phys. Oceanogr.*, *46*, 975–992, doi:10.1175/JPO-D-14-0187.1.

Deike, L. (2022), Mass transfer at the ocean–atmosphere interface: The role of wave breaking, droplets, and bubbles, *Ann. Rev. Fluid Mech.*, *54*, 191–224, doi:10.1146/annurev-fluid-030121-014132.

Demer, D., L. Berger, M. Bernasconi, E. Bethke, K. Boswell, D. Chu, and Domokos, R. et al. (2015), Calibration of acoustic instruments, *ICES CRR No. 326*, doi:10.25607/OBP-185.

Derakhti, M., and J. T. Kirby (2014), Bubble entrainment and liquid bubble interaction under unsteady breaking waves, *J. Fluid Mech.*, *761*, 464–506, doi:10.1017/jfm.2014.637.

Derakhti, M., and J. T. Kirby (2016), Breaking-onset, energy and momentum flux in unsteady focused wave packets, *J. Fluid Mech.*, *790*, 553–581, doi:10.1017/jfm.2016.17.

Derakhti, M., J. T. Kirby, F. Shi, and G. Ma (2016), Wave breaking in the surf zone and deep-water in a non-hydrostatic rans model. part 2: Turbulence and mean circulation, *Ocean Modelling*, *107*, 139–150, doi:10.1016/j.ocemod.2016.09.011.

Derakhti, M., M. L. Banner, and J. T. Kirby (2018), Predicting the breaking strength of gravity water waves in deep and intermediate depth, *J. Fluid Mech.*, *848*, doi:10.1017/jfm.2018.352.

Derakhti, M., J. Thomson, and J. T. Kirby (2020a), Sparse sampling of intermittent turbulence generated by breaking surface waves, *J Phys. Oceanogr.*, *50*(4), 867–885, doi:10.1175/JPO-D-19-0138.1.

Derakhti, M., J. T. Kirby, M. L. Banner, S. T. Grilli, and J. Thomson (2020b), A unified breaking-onset criterion for surface gravity water waves in arbitrary depth, *J. Geophys. Res.:Ocean*, *125*, doi:10.1029/2019JC015886.

Donelan, M., A. Babanin, E. Sanina, and D. Chalikov (2015), A comparison of methods for estimating directional spectra of surface waves, *Journal of Geophysical Research: Oceans*, pp. n/a–n/a, doi:10.1002/2015JC010808.

Felizardo, F., and W. Melville (1995), Correlation between ambient noise and the ocean surface wave field, *J. Phys. Oceanogr.*, *25*, 513–532.

Gemmrich, J. R., M. L. Banner, and C. Garrett (2008), Spectrally resolved energy dissipation rate and momentum flux of breaking waves, *J. Phys. Oceanogr.*, *38*, 1296–1312, doi:10.1175/2007JPO3762.1.

Hsu, S. (2003), Estimating overwater friction velocity and exponent of power-law wind profile from gust factor during storms, *J. Waterway, Port, Coastal, Ocean Eng.*, *129*, 174–177, doi:10.1061/(ASCE)0733-950X(2003)129:4(174).

Iyer, S., K. Drushka, E. J. Thompson, and J. Thomson (2022), Small-scale spatial variations of air-sea heat, moisture, and buoyancy fluxes in the tropical trade winds, *Journal of Geophysical Research: Oceans*, *127*(10), e2022JC018,972, doi:https://doi.org/10.1029/2022JC018972, e2022JC018972 2022JC018972.

Kleiss, J. M., and W. K. Melville (2010), Observations of wave breaking kinematics in fetch-limited seas, *J. Phys. Oceanogr.*, *40*, 2575–2604, doi:10.1175/2010JPO4383.1.

Kleiss, J. M., and W. K. Melville (2011), The analysis of sea surface imagery for whitecap kinematics, *Journal of Atmospheric and Oceanic Technology*, *28*(2), 219–243.

Lamarre, E., and W. Melville (1991), Air entrainment and dissipation in breaking waves, *Nature*, *351*, 469–472.

Lavery, A., C. Bassett, G. Lawson, and J. Jech (2017), Exploiting signal processing approaches from broadband echosounder, *ICES J. Mar. Sci.*, *75*(8), 2262–2275, doi:10.1093/icesjms/fsx155.

Malila, M. P., J. Thomson, Breivik, A. Benetazzo, B. Scanlon, and B. Ward (2022), On the Groupiness and Intermittency of Oceanic Whitecaps, *Journal of Geophysical Research: Oceans*, *127*(1), e2021JC017,938, doi:https://doi.org/10.1029/2021JC017938.

Manasseh, R., A. V. Babanin, C. Forbes, K. Rickards, I. Bobevski, and A. Ooi (2006), Passive Acoustic Determination of Wave-Breaking Events and Their Severity across the Spectrum, *J. Atmos. and Oceanic Tech.*, *23*, 599–618, doi:10.1175/JTECH1853.1.

Medwin, H. (1977), In situ acoustic measurements of microbubbles at sea, *J. Geophys. Res.*, *82*(6), 971–976, doi:10.1029/JC082i006p00971.

Medwin, H., and C. Clay (1998), *Fundamentals of Acoustics Oceanography*, 138-141 pp., Academic Press, Boston, MA.

Melville, W. K. (1996), The role of surface-wave breaking in air-sea interaction, *Ann. Rev. Fluid Mech.*, *28*, 279–321.

Melville, W. K., and P. Matusov (2002), Distribution of breaking waves at the ocean surface, *Nature*, *417*, 58–63.

Melville, W. K., F. Veron, and C. J. White (2002), The velocity field under breaking waves: coherent structures and turbulence, *J. Fluid Mech.*, *454*, 203–233, doi: 10.1017/S0022112001007078.

Monahan, E. C. (1969), Fresh water whitecaps, *J. Atmos. Sci.*, *26*, 1026–1029, doi: 10.1175/1520-0469(1969)026⟨1026:FWW⟩2.0.CO;2.

Monahan, E. C., and I. Muircheartaigh (1980), Optimal power-law description of oceanic whitecap coverage dependence on wind speed, *Journal of Physical Oceanography*, *10*, 2094–2099, doi:10.1175/1520-0485(1980)010⟨2094:OPLDOO⟩2.0.CO;2.

Perlin, M., W. Choi, and Z. Tian (2013), Breaking waves in deep and intermediate waters, *Annual Review of Fluid Mechanics*, *45*(1), 115–145, doi:10.1146/annurev-fluid-011212-140721.

Phillips, O., F. Posner, and J. Hansen (2001), High range resolution radar measurements of the speed distribution of breaking events in wind-generated ocean waves: Surface impulse and wave energy dissipation rates, *J Phys. Oceanogr.*, *31*, 450–460, doi: 10.1175/1520-0485(2001)031⟨0450:HRRRMO⟩2.0.CO;2.

Portilla, J., F. J. Ocampo-Torres, and J. Monbaliu (2009), Spectral partitioning and identification of wind sea and swell, *J. Atmosph. Oceanic Tech.*, *26*, 107–122, doi: 10.1175/2008JTECHO609.1.

Rapp, R. J., and W. K. Melville (1990), Laboratory measurements of deep-water breaking waves, *Phil. Trans R. Soc. Lond. A*, *331*, 735–800, doi:10.1098/rsta.1990.0098.

Renfree, J. S., L. N. Andersen, G. Macaulay, T. S. Sessions, and D. A. Demer (2020), Effects of sphere suspension on echosounder calibrations, *ICES Journal of Marine Science*, *77*(7-8), 2945–2953, doi:10.1093/icesjms/fsaa171.

Scanlon, B., and B. Ward (2016), The influence of environmental parameters on active and maturing oceanic whitecaps, *J. Geophys. Res.*, *121*, 3325–3336, doi: 10.1002/2015JC011230.

Schwendeman, M., and J. Thomson (2015a), Observations of whitecap coverage and the relation to wind stress, wave slope, and turbulent dissipation, *J. Geophys. Res.: Oceans*, *120*, 8346–8363, doi:10.1002/2015JC011196.

Schwendeman, M., and J. Thomson (2015b), A horizon-tracking method for shipboard video stabilization and rectification, *Journal of Atmospheric and Oceanic Technology*, *32*(1), 164–176.

Schwendeman, M., J. Thomson, and J. Gemmrich (2014), Wave breaking dissipation in a young wind sea, *J. Phys. Oceanogr.*, *44*, 104–127, doi:10.1175/JPO-D-12-0237.1.

Stanton, T. K., and D. Chu (2008), Calibration of broadband active acoustic systems using a single standard spherical target, *The Journal of the Acoustical Society of America*, *124*(1), 128–136, doi:10.1121/1.2917387.

Strand, K. O., Ø. Breivik, G. Pedersen, F. B. Vikebø, S. Sundby, and K. H. Christensen (2020), Long-term statistics of observed bubble depth versus modeled wave dissipation, *J. Geophys. Res.: Oceans*, *125*, e2019JC015,906, doi:10.1029/2019JC015906.

Sugihara, Y., H. Tsumori, T. Ohga, H. Yoshioka, and S. Serizawa (2007), Variation of whitecap coverage with wave-field conditions, *J Marine Sys.*, *66*, 47–60, doi: 10.1016/j.jmarsys.2006.01.014.

Sullivan, P. P., and J. C. McWilliams (2010), Dynamics of winds and currents coupled to surface waves, *Ann. Rev. Fluid Mech.*, *42*, 19–42, doi:10.1146/annurev-fluid-121108-145541.

Sutherland, P., and W. K. Melville (2013), Field measurements and scaling of ocean surface wave-breaking statistics, *Geophys. Res. Let.*, pp. 3074–3079, doi:10.1002/grl.50584.

Terrill, E. J., W. K. Melville, and D. Stramski (2001), Bubble entrainment by breaking waves and their influence on optical scattering in the upper ocean, *J. Geophys. Res.: Oceans*, *106*, 16,815–16,823, doi:10.1029/2000JC000496.

Thomson, J. (2012), Wave breaking dissipation observed with SWIFT drifters, *J. Atmos. Oceanic Technol.*, *29*, 1866–1882, doi:10.1175/JTECH-D-12-00018.1.

Thomson, J., and A. Jessup (2009), A fourier-based method for the distribution of breaking crests from video observations, *J. Atmos. Ocean. Tech.*, *26*, 1663–1671, doi: 10.1175/2009JTECHO622.1.

Thomson, J., M. S. Schwendeman, S. F. Zippel, S. Moghimi, J. Gemmrich, and W. E. Rogers (2016), Wave-breaking turbulence in the ocean surface layer, *J. Phys. Oceanogr.*, *46*, 1857–1870, doi:10.1175/JPO-D-15-0130.1.

Thomson, J., J. B. Girton, R. Jha, and A. Trapani (2018), Measurements of directional wave spectra and wind stress from a wave glider autonomous surface vehicle, *J. Atm. Oceanic Tech.*, *35*(2), 347–363, doi:10.1175/JTECH-D-17-0091.1.

Thomson, J., M. Moulton, A. de Klerk, J. Talbert, M. Guerra, S. Kastner, M. Smith, M. Schwendeman, S. Zippel, and S. Nylund (2019), A new version of the swift platform for waves, currents, and turbulence in the ocean surface layer, in *IEEE/OES Workshop on Currents, Waves, and Turbulence Measurements*.

Thorpe, S. (1982), On the clouds of bubbles formed by breaking wind-waves in deep water, and their role in air-sea gas transfer, *Phil. Tran. R. Soc. Lond. A*, *304*, 155–210, doi: 10.1098/rsta.1982.0011.

Thorpe, S. (1986), Measurements with an automatically recording inverted echo sounder; aries and the bubble clouds, *J. Phys. Oceanogr.*, *16*, 1462–1478, doi: 10.1175/1520-0485(1986)016⟨1462:MWAARI⟩2.0.CO;2.

Thorpe, S. (1992), Bubble clouds and the dynamics of the upper ocean, *Quart. J. Roy. Meteor. Soc.*, *118*, 1–22, doi:10.1002/qj.49711850302.

Trevorrow, M. (2003), Measurements of near-surface bubble plumes in the open ocean with implications for high-frequency sonar performance, *J. AcousṠoc. Am.*, *114*(5), 2672–2684, doi:10.1121/1.1621008.

Vagle, S., and D. Farmer (1998), A comparison of four methods for bubble size and void fraction measurements, *IEEE Journal of Oceanic Engineering*, *23*(3), 211–222, doi: 10.1109/48.701193.

Vagle, S., C. McNeil, and N. Steiner (2010), Upper ocean bubble measurements from the ne pacific and estimates of their role in air-sea gas transfer of the weakly soluble gases nitrogen and oxygen, *J. Geophys. Res.: oceans*, *115*, doi:10.1029/2009JC005990.

Vagle, S., J. Gemmrich, and H. Czerski (2012), Effect of upper ocean stratification on turbulence and optically active bubbles, *J. Geophys. Res.*, *117*(C00H16), doi: 10.1029/2011JC007308.

Wang, D. W., H. W. Wijesekera, E. Jarosz, W. J. Teague, and W. S. Pegau (2016), Turbulent diffusivity under high winds from acoustic measurements of bubbles, *J. Phys. Oceanogr.*, *46*, 1593–1613, doi:10.1175/JPO-D-15-0164.1.

Yelland, M., P. Taylor, I. Consterdine, and M. Smith (1994), The use of the inertial dissipation technique for shipboard wind stress determination, *J. Atmos. Ocean. Tech.*, *11*, 1093–1108.

Zhao, D., and Y. Toba (2001), Dependence of whitecap coverage on wind and wind-wave properties, *J. Oceanogr.*, *57*, 603–616, doi:10.1023/A:1021215904955.

Zippel, S. F., T. Maksym, M. Scully, P. Sutherland, and D. Dumont (2020), Measurements of enhanced near-surface turbulence under windrows, *Journal of Physical Oceanography*, *50*(1), 197–215, doi:10.1175/JPO-D-18-0265.1.

Figure.

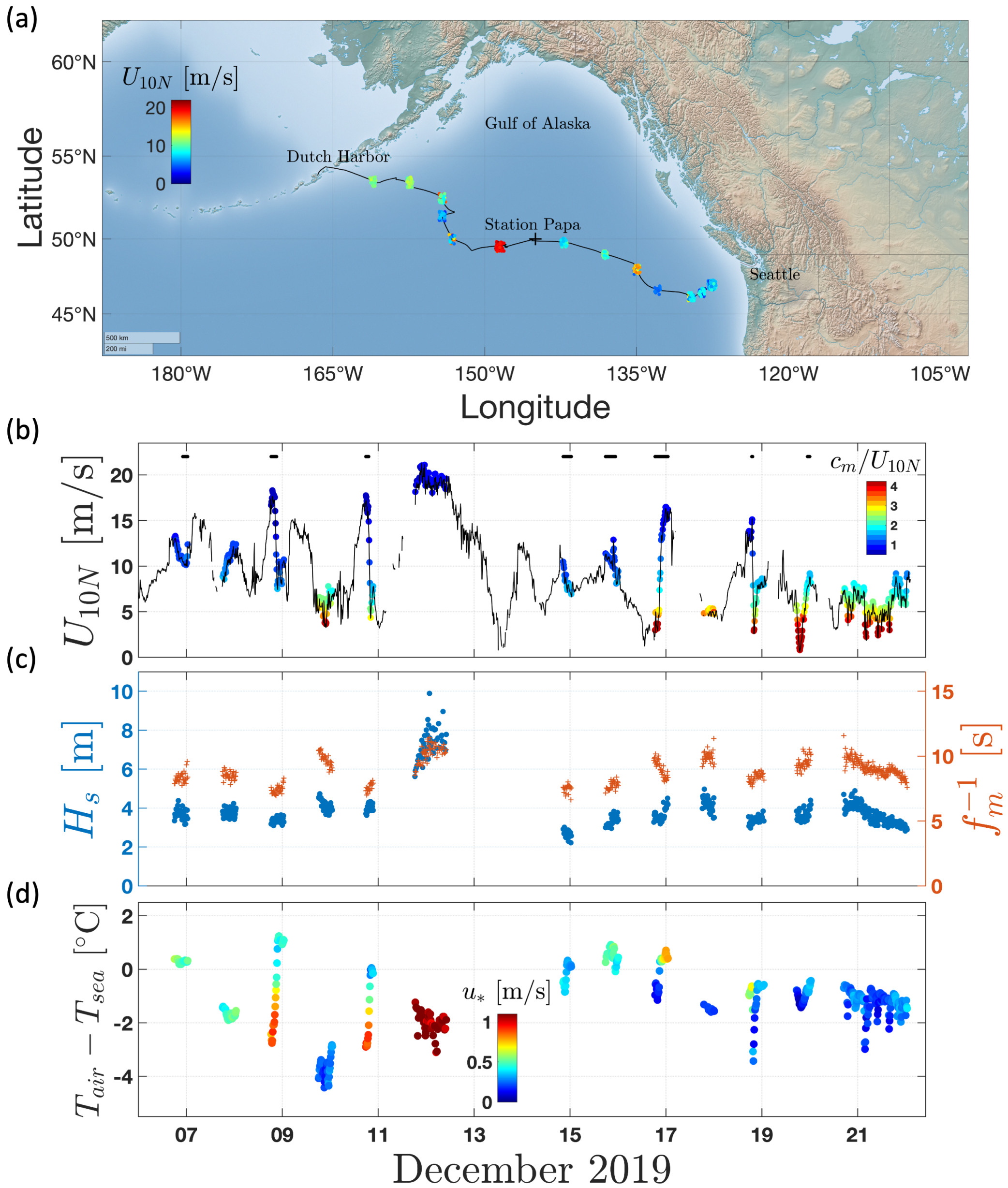

Figure A.1: Overview of (a) the cruise track (solid line) and average location of the drifting SWIFT buoys (circles) during each deployment along the transit, and $(b - d)$ the observed range of environmental conditions. Here U_{10N}, H_s, f_m, T_{air}, and T_{sea} represent 10-minute average neutral wind speed at 10 m above the sea surface, significant wave height, spectrally-averaged wave frequency, and air and water temperature, respectively. The color code in (b) and (d) shows the wave age and the air-side friction velocity, respectively. In (b), the horizontal line segments indicate the intervals during which data were collected in the presence of persistent rain (rain rates have not been measured). Local water depths during most of the deployments were greater than 4000 m.

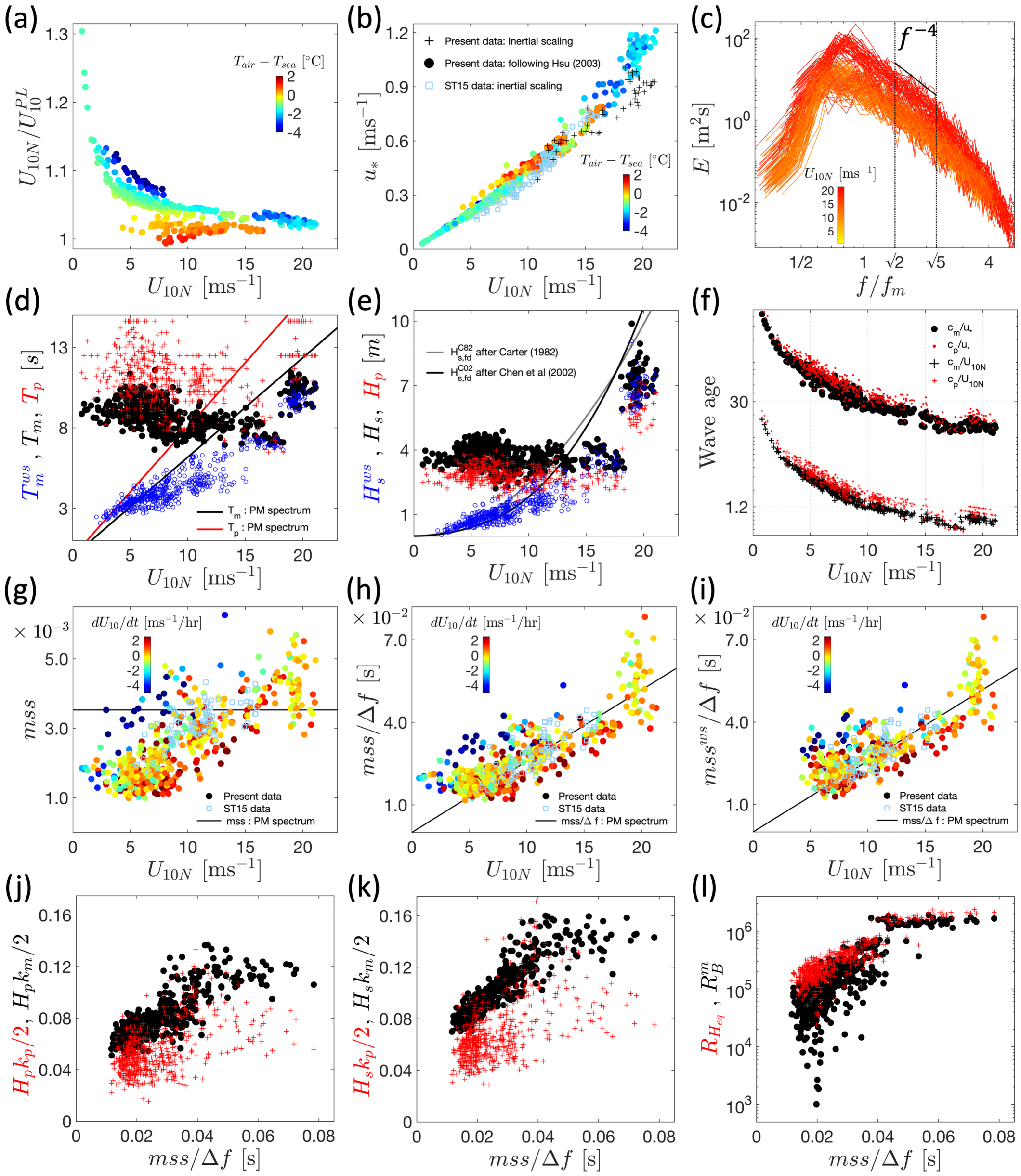

Figure A.2: Observed range of wind and wave statistics against U_{10N} and equilibrium-range mean square slope $mss/\Delta f$ (Eq. 2). All variables are defined in §2.2 and §2.3.

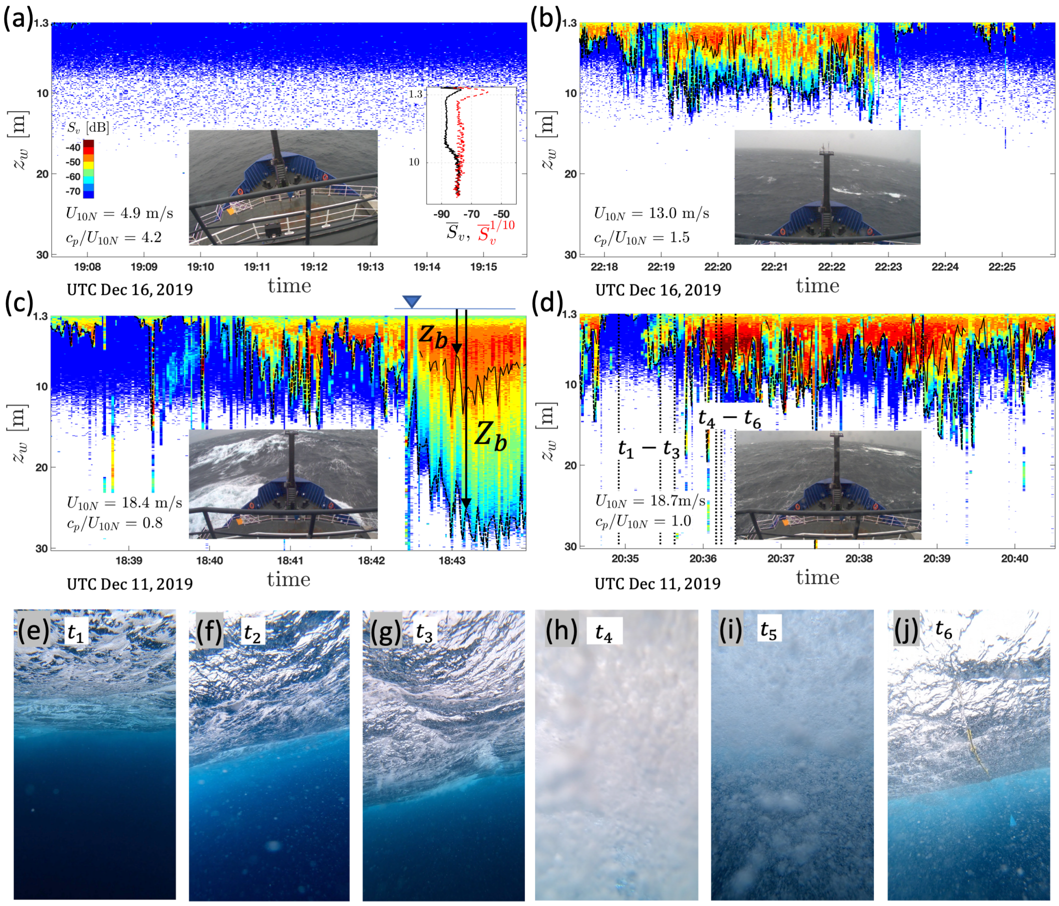

Figure A.3: Examples of a depth-time map (echogram) of the volume backscattering strength S_v [dB] in $(a - b)$ a rapidly evolving sea with different sea state conditions (but steady rain) on UTC Dec 16 and in $(c-d)$ a storm with sustained wind speeds of $U_{10N} > 18.0$ ms^{-1} on UTC Dec 11. In (a), the signal represents observations just after a steady calm sea state with minimum whitecapping and is expected to be mainly from scattering particles or bubbles not associated with breaking waves. The sub-surface optical images in $(e - j)$ correspond to the time instants $t_1 - t_6$ marked by the vertical dashed lines in (d) and are collected by a GoPro camera mounted on the SWIFT buoy. Above-surface optical images in $(a-d)$, taken from a camera on the ship's bridge, show a snapshot of the surface wave field within the time range of the corresponding echogram. Dotted-dashed and solid contours indicate Z_b and z_b, the two estimates of the local penetration depth of entrained bubbles defined in § 2.5. Echograms are collected by a downward-looking echosounder integrated on SWIFT buoys in a surface-following reference frame z_w, where z_w is positive downward, and $z_w = 0$ represents the instantaneous free surface level.

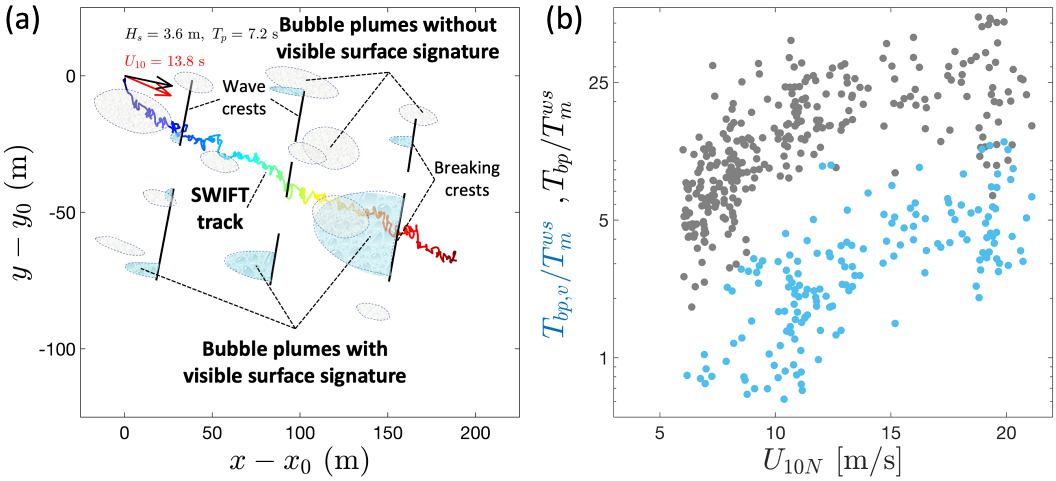

Figure A.4: (a) Schematic of a SWIFT track (with respect to the earth frame) drifting across an intermittent field of bubble clouds during a 512-s burst, along which echogram data are collected in a surface following reference frame, and (b) apparent residence time of bubble clouds in echogram data against wind speeds. In (a), (x_0, y_0) is the initial horizontal location of the buoy, and the black and red arrows show the dominant wave and wind directions, respectively. Subscripts bp and bp, v denote the statistics corresponding to the bubble plumes obtained from the thresholding methods BDM1 and BDM2 (described in §2.5), respectively.

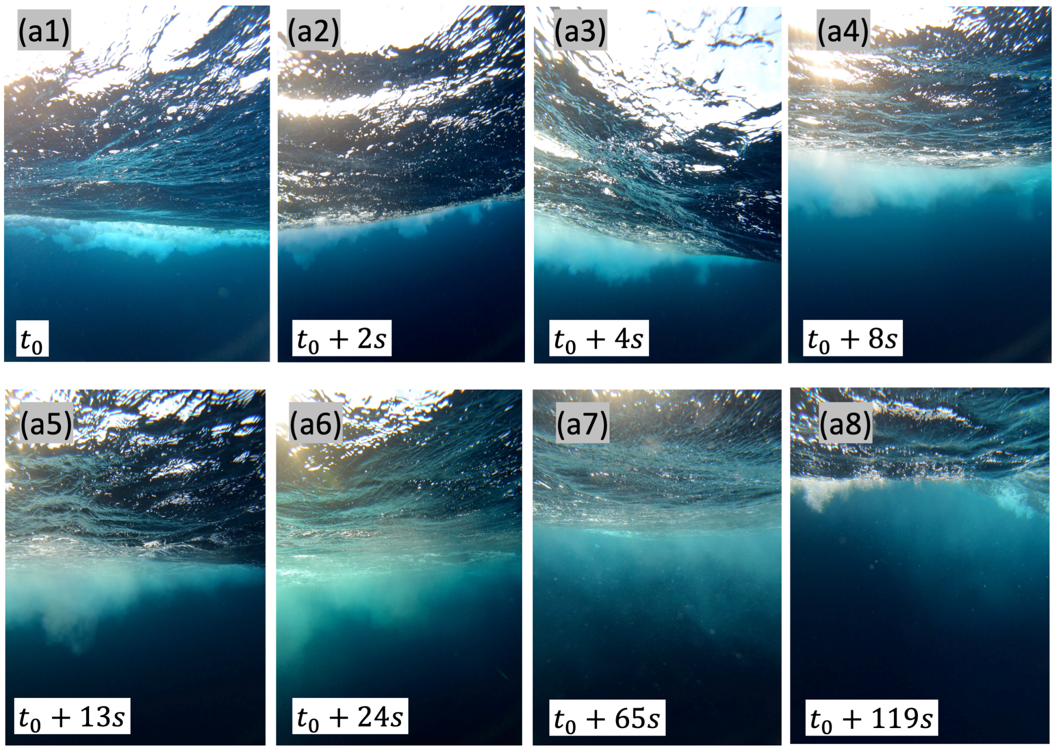

Figure A.5: Example sub-surface images collected by a GoPro camera on a SWIFT buoy showing the sub-surface visible signature of an evolving bubble plume in an old sea with moderate wind speeds of $U_{10N} \approx 11$ ms^{-1}.

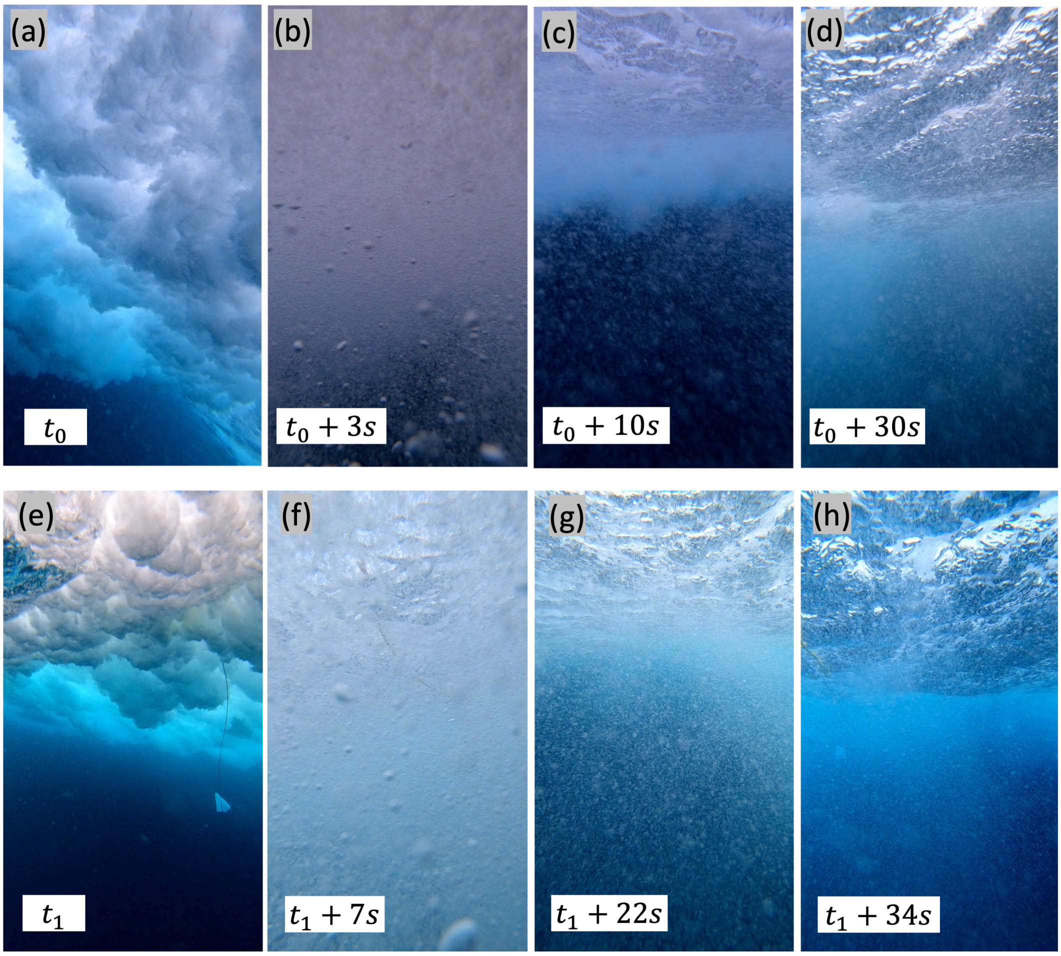

Figure A.6: Example sub-surface images collected by a GoPro camera on a SWIFT buoy showing the sub-surface visible signature of two different evolving bubble plumes in a storm with sustained wind speeds of $U_{10N} > 18$ ms^{-1}.

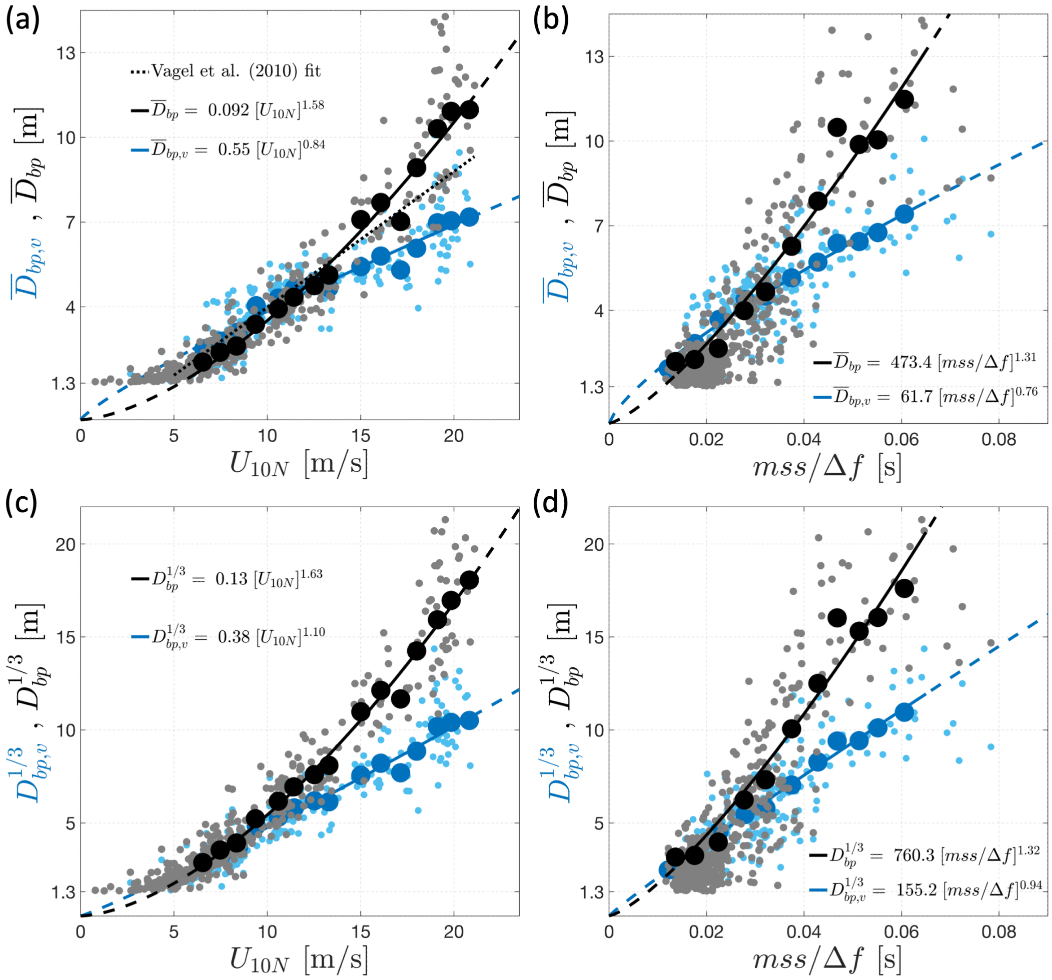

Figure A.7: Observed range of $(a - b)$ mean (Eq. 6) and $(c - d)$ significant (Eq. 7) bubble plume depths against wind speed U_{10N} and the equilibrium range $mss/\Delta f$. Fits are obtained from the least squares fitting to the binned data points (large circles). Subscripts bp and bp, v denote the statistics corresponding to the bubble plumes obtained from the thresholding methods BDM1 and BDM2 (described in §2.5), respectively.

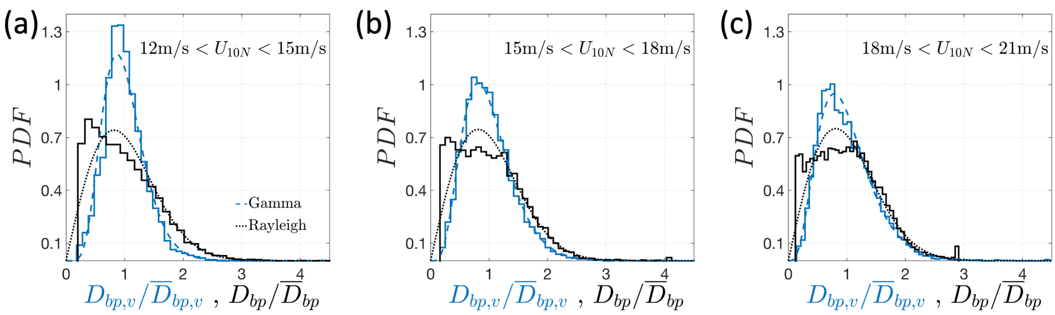

Figure A.8: Probability distribution function, PDF, of the estimated bubble depths at different wind speed ranges. Dotted and dashed lines show the fitted Rayleigh and Gamma distributions to the observed PDFs.

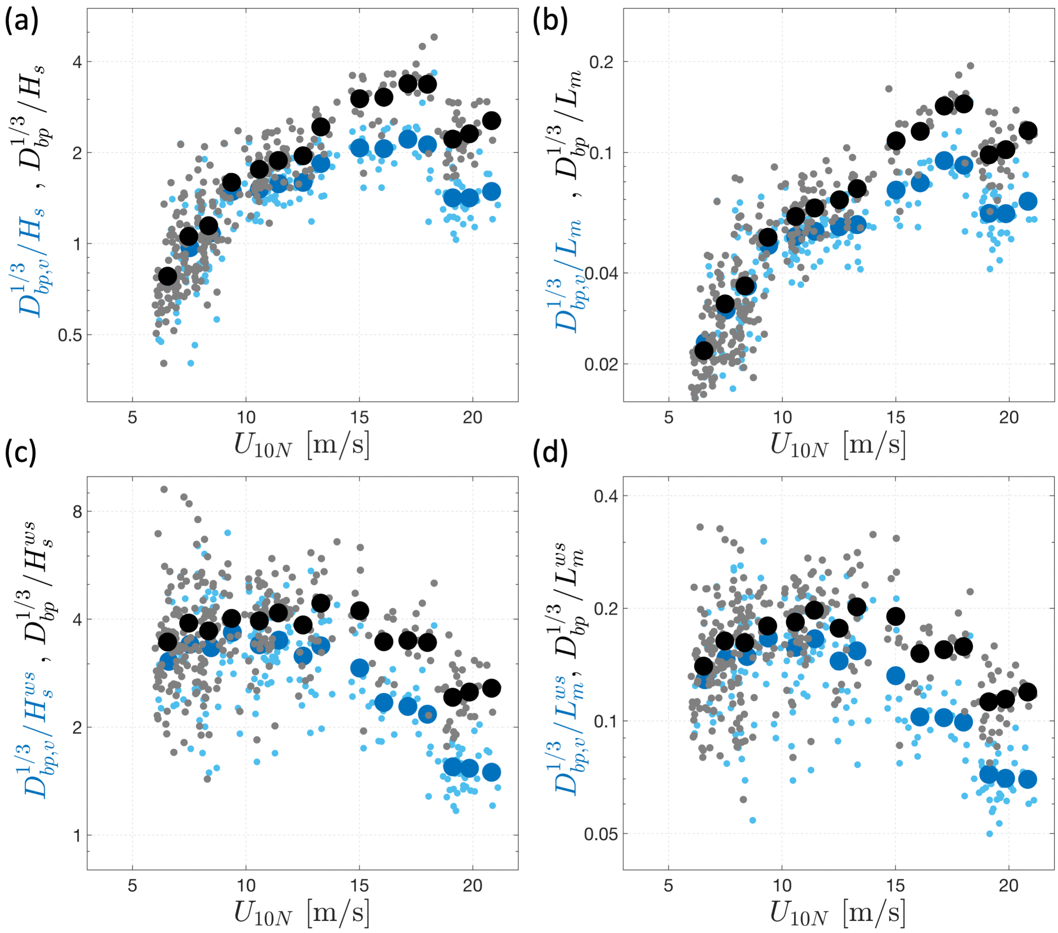

Figure A.9: Scaled bubble plume penetration depths against wind speeds. Here H_s is the total significant wave height, $L_m = g/2\pi * T_m^2$ is the total mean wavelength, H_s^{ws} is the wind sea significant wave height, $L_m^{ws} = g/2\pi * (T_m^{ws})^2$ is the wind sea mean wavelength, all defined in §2.3. Large circles represent the binned data points. Subscripts bp and bp, v denote statistics correspond to the bubble plumes obtained from the thresholding methods BDM1 and BDM2 (described in §2.5), respectively.

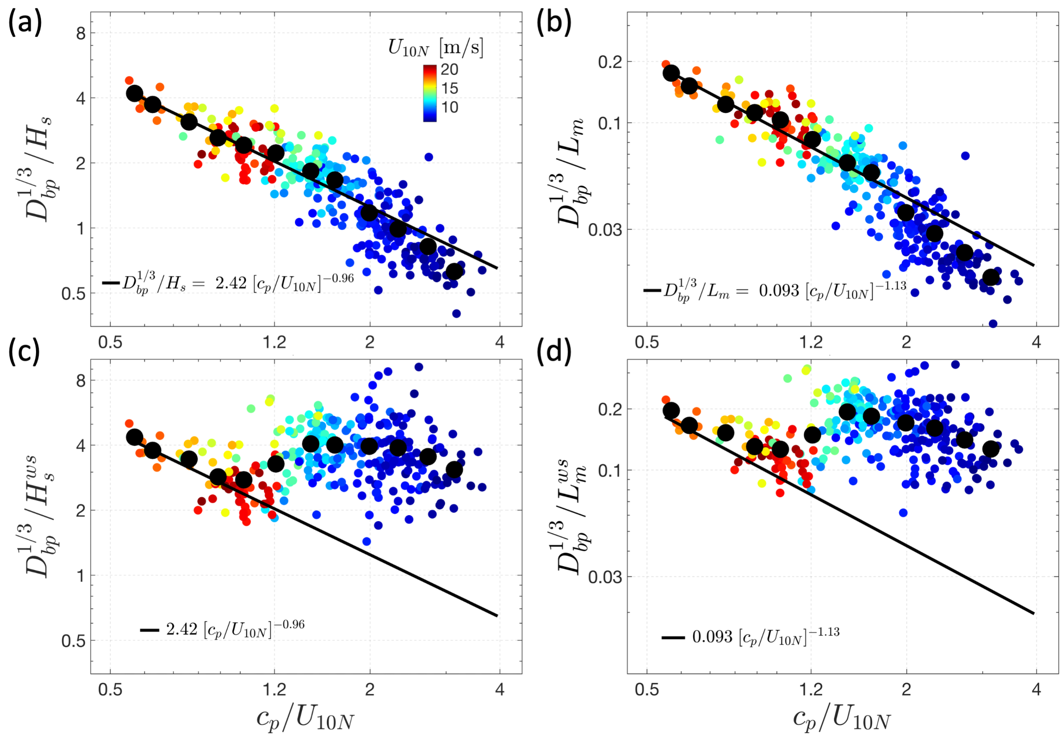

Figure A.10: Scaled bubble plume depths against wave age colored by wind speed. In (a) and (b), the fits are obtained from the least squares fitting to the binned data points (large circles). Definitions are as in Figure A.9.

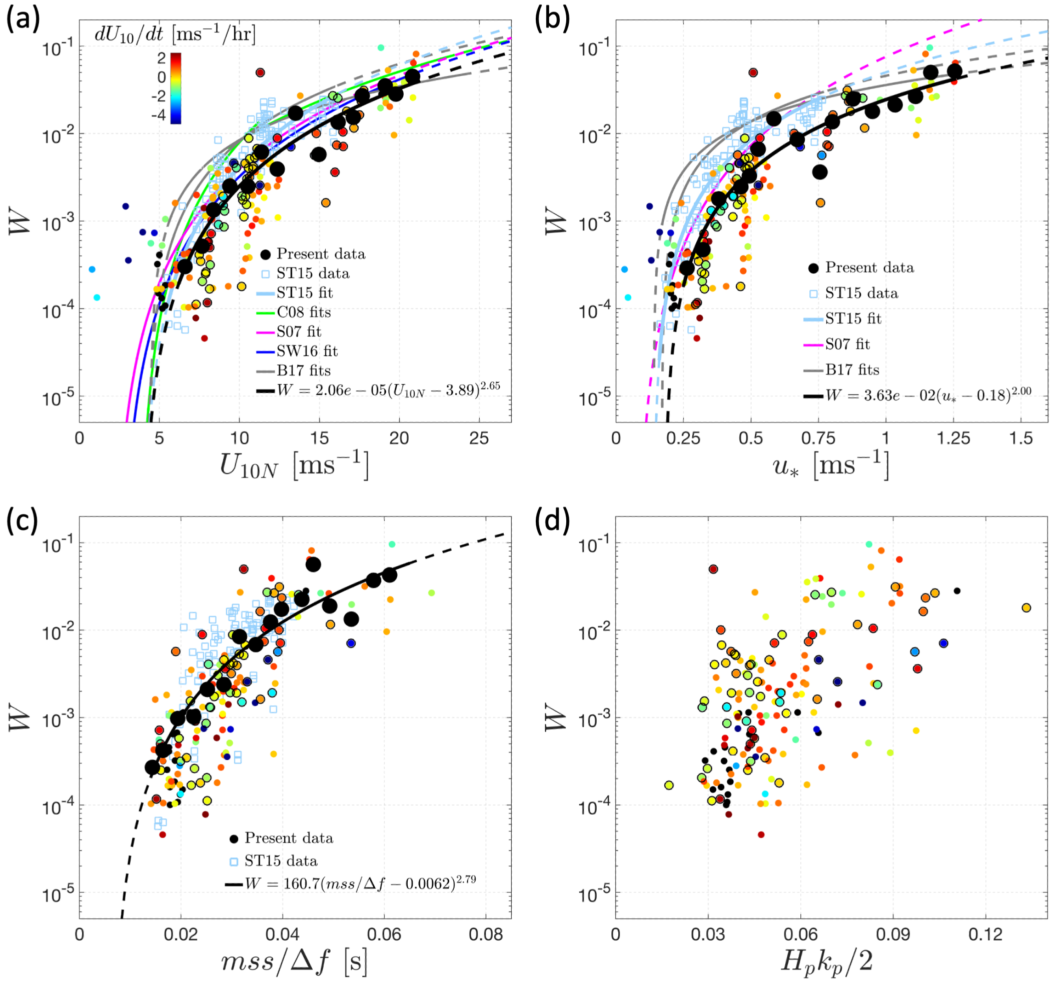

Figure A.11: Observed range of whitecap coverage against (a) wind speed U_{10N}, (b) air friction velocity u_*, (c) the equilibrium range $mss/\Delta f$, and (d) the significant spectral peak steepness $H_p k_p/2$, all colored by the wind accelerations dU_{10N}/dt (all defined in §2). Circles with black edges represent the data in the presence of rain (rain rates have not been measured). The best fits to the present data are obtained from the least squares fitting to the bin-averaged data points (large black circles).

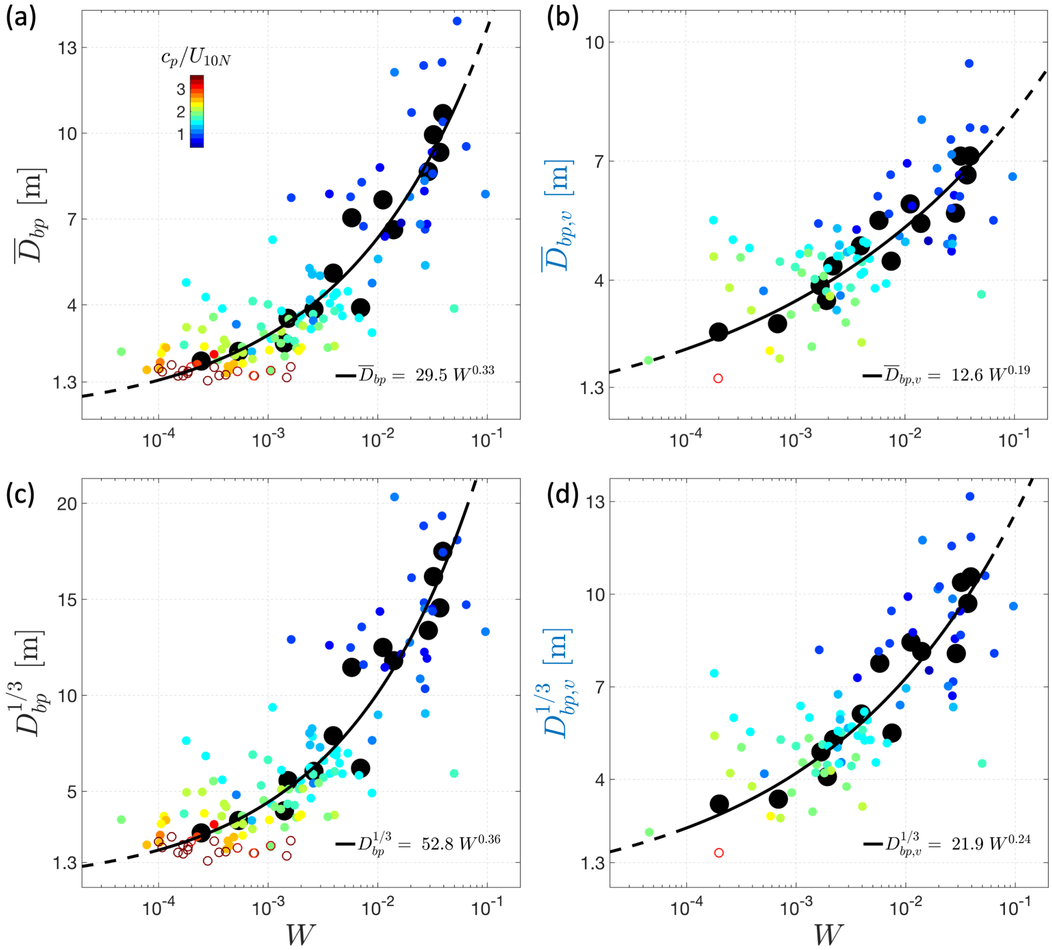

Figure A.12: Mean and significant bubble plume depths against whitecap coverage. The best fits to the present data are obtained from the least squares fitting to the bin-averaged data points as a function of U_{10N} (large black circles). Open circles represent the data with U_{10N} < 6 ms^{-1}.

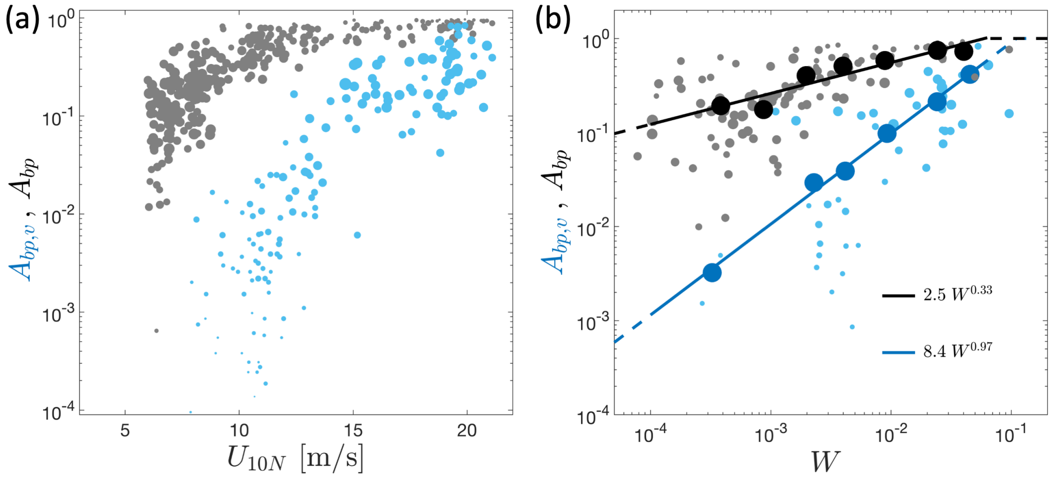

Figure A.13: Proxy for the fractional area of the bubble plumes against (a) wind speed and (b) whitecap coverage. Symbol sizes are a function of the number of bubble clouds detected in a burst averaged over concurrent (1 to 4) bursts ranging from 0.5 to 26. In (b), large symbols represent the corresponding binned data with more than three detected bubble clouds in a burst. Subscripts bp and bp, v denote the statistics corresponding to the bubble plumes obtained from the thresholding methods BDM1 and BDM2 (described in §2.5), respectively.